

Numerical aspects of Casimir energy computation in acoustic scattering

Timo Betcke^a, Alexander Strohmaier^b, Xiaoshu Sun^{a,*}

^a*Department of Mathematics, University College London, London, WC1E 6BT, UK*

^b*School of Mathematics, University of Leeds, Leeds, LS2 9JT, UK*

Abstract

Computing the Casimir energy is a classical problem of quantum electrodynamics going back to the 1940s. In the early two thousands a significant breakthrough was achieved by representing the Casimir energy as the computation of the integral of the log determinant of certain boundary integral operators in the complex plane. Recently, this log determinant formula was investigated in the context of the Krein spectral shift function, which suggests a potential alternative computational approach based on the numerical evaluation of scattering matrices. In this paper, we will give an overview of these computational techniques of computing the Casimir energy in three dimensional acoustic scattering. Afterwards, we will discuss the spectral properties of the block matrices inside the formula of the Casimir energy, which are constructed by the integral operators and investigate how to use these properties to speed up Casimir computations for large-scale practical problems.

Keywords: Krein spectral shift function, Casimir energy, Krylov subspace, inverse-free generalized eigenvalue problem, Bempp

1. Introduction

Since late 1940s, the advanced understanding of vacuum sector of quantum electrodynamics has been developed and one of the most seminal predictions is the vacuum effects (quantum fluctuations of the electromagnetic field) can induce attractive forces between two uncharged, perfectly conducting, parallel plates. This phenomenon is called *Casimir effect*, which is firstly proposed by H.B.G. Casimir in 1940s [1]. To obtain the formula of the Casimir energy, he considered the space between these two plates as a type of electromagnetic cavity, solved the classical Maxwell equations with certain boundary condition for all the valid excitations of the electromagnetic field in this cavity and obtained countably infinite electromagnetic mode frequencies $\{\omega_n(a)\}$, where a is the surface-surface distance. Accordingly, the electromagnetic zero-point energy of the n th cavity mode is $\frac{\hbar\omega_n(a)}{2}$ and by summing up all the contributions from the modes, he finally get the expression of the *Casimir energy*:

$$\mathcal{E}(a) = \frac{1}{2} \sum_n \hbar\omega_n(a),$$

which is divergent. However, Casimir derived a finite result for the derivative of this infinite energy fluctuations, which is the *Casimir force per unit area*:

$$F(a) = -\frac{1}{A} \frac{\partial \mathcal{E}}{\partial a} = -\frac{\hbar c \pi^2}{240 a^4},$$

where A is the cross-sectional area of the boundary plates.

In 1960s, Lifshitz generalized this theory to the case of dielectric media [2], which means the boundary surfaces are not perfect conductors but the real-world materials such as the solid consisting of the atomic

*Corresponding author

URL: t.betcke@ucl.ac.uk (Timo Betcke), a.strohmaier@leeds.ac.uk (Alexander Strohmaier), xiaoshu.sun.18@ucl.ac.uk (Xiaoshu Sun)

constituents. He proposed that any microscopic volume ΔV of the plates contains a collection of atomic-scale electric dipoles without uniform orientation due to the absence of the external forcing field. Once in a while, the quantum and thermal fluctuations may make the dipoles align spontaneously, resulting in a net electric dipole moment. It is like van der Waals interaction between the atoms and this dipole moment induces a net dipole field. Meanwhile, the dipoles in the opposite plate feel this field across the gap and align as well. Now, there are two net electric dipole moments which make two plates attract with each other. Lifshitz emphasized the influence from the materials more than the fluctuations in the empty space between the plates and this interpretation provides little advantage on the computation of the Casimir energy since it is unknown on how to compute each contribution from the volume ΔV .

Afterwards, there is a decades absence of experimental input on the Casimir effect and finally in 1996, the precise measurements of the Casimir force between the extended bodies have been done by S.K. Lamoreaux [3]. From 2000 to 2008, the Casimir force has been measured in various experimental configurations, such as cylinder-cylinder [4], plate-plate [5], sphere-plate [6] and sphere-comb [7]. The rapid growth in experimental investigation is followed by the theoretical development. From 2007 to 2008, the asymptotic series of the Casimir energy have been explicitly computed in both scalar [8] and vector [9] cases. In 2009, the authors of [10] put forward a method of computing the Casimir interactions between arbitrary three-dimensional objects with arbitrary material properties [10], in which the Casimir energy between the perfectly conducting compact objects can be described as:

$$\mathcal{E} = -\frac{\hbar c}{2\pi} \int_0^\infty dk \log \frac{\mathcal{Z}(k)}{\mathcal{Z}_\infty(k)},$$

where

$$\mathcal{Z}(k) = \int \mathcal{D}\mathbf{J}(\mathbf{x}) e^{\frac{i}{2} \int \int d\mathbf{x} d\mathbf{y} \mathbf{J}(\mathbf{x}) \cdot \mathbf{G}_k(\mathbf{x}, \mathbf{y}) \cdot \mathbf{J}(\mathbf{y})} \quad (1)$$

is a functional integration extending over all possible surface current distributions $\mathbf{J}(\mathbf{x})$ on the objects and $\mathcal{Z}_\infty(k)$ is $\mathcal{Z}(k)$ computed with all the objects removed to infinite separation. Moreover, in (1),

$$\mathbf{G}_k(\mathbf{x}, \mathbf{y}) = \left[1 + \frac{1}{k^2} \nabla_{\mathbf{x}} \otimes \nabla_{\mathbf{y}} \right] \frac{e^{ik|\mathbf{x}-\mathbf{y}|}}{4\pi|\mathbf{x}-\mathbf{y}|}$$

is the dyadic/tensor Green's function and k is the wavenumber. Johnson proposed that one could formally apply contour integral arguments to obtain the integral along the imaginary axis on which the integrand is nicely behaved (non-oscillatory and exponentially decaying). In this case, the Casimir energy formula is rewritten as

$$\mathcal{E} = -\frac{\hbar c}{2\pi} \int_0^\infty dk \log \frac{\mathcal{Z}(ik)}{\mathcal{Z}_\infty(ik)}, \quad (2)$$

where

$$\mathcal{Z}(ik) = \int \mathcal{D}\mathbf{J}(\mathbf{x}) e^{\frac{i}{2} \int \int d\mathbf{x} d\mathbf{y} \mathbf{J}(\mathbf{x}) \cdot \mathbf{G}_{ik}(\mathbf{x}, \mathbf{y}) \cdot \mathbf{J}(\mathbf{y})} \quad (3)$$

and

$$\mathbf{G}_{ik}(\mathbf{x}, \mathbf{y}) = \left[1 - \frac{1}{k^2} \nabla_{\mathbf{x}} \otimes \nabla_{\mathbf{y}} \right] \frac{e^{-k|\mathbf{x}-\mathbf{y}|}}{4\pi|\mathbf{x}-\mathbf{y}|}.$$

This \mathbf{G}_{ik} is called the Wick-rotated dyadic/tensor Green's function. One can notice that this Green's function is strongly singular due to the second order form $(\nabla_{\mathbf{x}} \otimes \nabla_{\mathbf{y}})$.

However, a more rigorous mathematical derivation was recently provided by Hanisch, Strohmaier and Waters [11] who have shown that the natural and well-defined object is the integral along the imaginary axis. They

also provided a mathematical framework to connect the integral to families of trace formulas and the Casimir energy is one of the examples. To be specific, by assuming that the objects Ω is assembled from individual objects Ω_j , for $j = 1, \dots, N$ and $\partial\Omega_j$ are the N connected components of the boundary $\partial\Omega$. Then, several self-adjoint operators on $L^2(\mathbb{R}^d)$ can be defined for constructing the *Birman-Krein formula* later:

- The operator Δ is the Laplace operator with Dirichlet boundary conditions on $\partial\Omega$.
- For $j = 1, \dots, N$, the operator Δ_j is the Laplace operator with Dirichlet boundary conditions on $\partial\Omega_j$.
- The operator Δ_0 is the ‘free’ Laplace operator on \mathbb{R}^d with domain $H^2(\mathbb{R}^d)$.

Now, the Birman-Krein formula can be written as

$$\text{Tr} \left(f(\Delta^{\frac{1}{2}}) - f(\Delta_0^{\frac{1}{2}}) - \left(\sum_{j=1}^N [f(\Delta_j^{\frac{1}{2}}) - f(\Delta_0^{\frac{1}{2}})] \right) \right) = \int_0^\infty f'(k) \xi(k) dk, \quad (4)$$

where

$$\xi(k) = \frac{1}{2\pi i} \log \left(\frac{\det(S(k))}{\det(S_{1,k}) \cdots \det(S_{N,k})} \right)$$

is called the *relative Krein spectral shift function* (KSSF). Here, $S_{j,k}$ are the scattering matrices of Δ_j associated to the objects Ω_j .

According to [11], by setting $f(x) = x$, (4) becomes

$$\text{Tr} \left(\Delta^{\frac{1}{2}} + (N-1)\Delta_0^{\frac{1}{2}} - \sum_{j=1}^N \Delta_j^{\frac{1}{2}} \right) = \int_0^\infty \xi(k) dk \quad (5)$$

and the value of the integral in (5) is the Casimir energy. However, this integral is not Lebesgue integrable and therefore cannot be used to compute the energy. To solve this problem, the authors derivate a relation between the KSSF and the integral operators and finally make the Casimir energy numerically computable via the integral operator method.

In this paper, we are going to introduce the numerical framework of computing the Casimir energy based on the evaluation of the log determinant of the integral operators in the acoustic case ¹ in Section 2 and discuss the spectral properties of the block matrices constructed from the integral operators in Section 3. Afterwards, with these properties, two efficient methods for computing the integrand of the Casimir energy will be illustrated in Section 4 which makes us compute the large-scale problem efficiently. In Section 5, several examples on computing the Casimir energy between the compact objects will be shown and we will also compare our results with others computed in other methods. Note that all the tests and examples in this paper were computed with version 3.3.4 of the BEM++ library [12]. Finally, Section 6 will conclude our paper and discuss the future plan as well.

2. Numerical methods for computing the Casimir energy in acoustic scattering

In this section, we are going to investigate the numerical methods on computing the Casimir energy. We would like to use the following notations for the domains of the boundary integral operators in both scalar and vector case. Assume $\Omega^- \in \mathbb{R}^d$, for $d \geq 2$ is the interior bounded Lebesgue-measurable domain that the scatterer occupies with Lipschitz-continuous boundary Γ and $\Gamma := \partial\Omega$ has a finite number of smooth faces that meet

¹The mathematical theories and numerical experiments in the Maxwell case have been done as well and they will be reported in another paper.

at non-degenerate edges and corners. In addition, the exterior domain is denoted as $\Omega^+ = \mathbb{R}^d \setminus \overline{\Omega^-}$. \mathbf{n} is the exterior unit normal to the surface Γ pointing outwards from Ω^- and $\mathbf{n}_{\mathbf{x}}$ is normal to Γ at the point $\mathbf{x} \in \Gamma$.

In the scalar case, the Casimir energy can be expressed in terms of the single-layer boundary operator and we will start from defining the function space on which the boundary operators are well-defined and Dirichlet trace operator, then give the definition of the single-layer boundary operator. Afterwards, the relation between the Krein spectral shift function with this operator will be introduced and finally, the numerical framework for computing the Casimir energy in the scalar case via the Galerkin discretization of the single-layer boundary operator.

2.1. Scalar function space and trace operator

For the bounded interior domain Ω^\pm or the unbounded exterior domain Ω^+ , the space of the square integrable functions is

$$L^2(\Omega^\pm) := \left\{ f : \Omega^\pm \rightarrow \mathbb{C}, f \text{ is Lebesgue measurable and } \int_{\Omega^\pm} |f|^2 < \infty \right\}$$

and the Sobolev space $H^s(\Omega^\pm)$ is defined as

$$H^s(\Omega^\pm) := \{ f \in L^2(\Omega^\pm), \forall \alpha \text{ s.t. } |\alpha| \leq s, D^\alpha f \in L^2(\Omega^\pm) \},$$

where $\alpha = (\alpha_1, \alpha_2, \dots, \alpha_d)$ is a multi-index and $|\alpha| = \alpha_1 + \alpha_2 + \dots + \alpha_d$, and the derivative is defined in the weak sense.

To construct the single-layer boundary operator, we also need the Dirichlet trace operator $\gamma_D^\pm : H^1(\Omega^\pm) \rightarrow H^{\frac{1}{2}}(\Gamma)$: for sufficiently smooth function p ,

$$\gamma_D^\pm p(\mathbf{x}) := \lim_{\Omega^\pm \ni \mathbf{x}' \rightarrow \mathbf{x} \in \Gamma} p(\mathbf{x}'),$$

where the subscripts $-$ and $+$ denote the interior and exterior traces, respectively.

2.2. Single-layer boundary integral operator

Typically, the *single-layer potential operator* $\mathcal{V}_k : H^{-\frac{1}{2}}(\Gamma) \rightarrow H^1(\Omega^\pm)$ can be represented as

$$(\mathcal{V}_k \mu)(\mathbf{x}) := \int_{\Gamma} g_k(\mathbf{x}, \mathbf{y}) \psi(\mathbf{y}) dS_{\mathbf{y}}, \quad \text{for } \mu \in H^{-\frac{1}{2}}(\Gamma) \text{ and } \mathbf{x} \in \Omega^\pm \setminus \Gamma,$$

where $g_k(\mathbf{x}, \mathbf{y})$ is the fundamental solution of the Helmholtz operator and especially,

$$g_k(\mathbf{x}, \mathbf{y}) = \begin{cases} \frac{i}{4} H_0^{(1)}(k|\mathbf{x} - \mathbf{y}|), & \text{for } d = 2 \\ \frac{e^{ik|\mathbf{x} - \mathbf{y}|}}{4\pi|\mathbf{x} - \mathbf{y}|}, & \text{for } d = 3, \end{cases} \quad (6)$$

where $H_0^{(1)}$ is a Hankel function of the first kind.

Now we can derive the *single-layer boundary operator* $V_k : H^{-\frac{1}{2}}(\Gamma) \rightarrow H^{\frac{1}{2}}(\Gamma)$ from this potential operator:

$$(V_k \mu)(\mathbf{x}) := \{\gamma_D \mathcal{V}_k \mu\}_{\Gamma}(\mathbf{x}).$$

Combining with the jump condition

$$[\gamma_D]_{\Gamma} \mathcal{V}_k = \gamma_D^+ \mathcal{V}_k - \gamma_D^- \mathcal{V}_k = 0,$$

we can derive that

$$\gamma_D^+ \mathcal{V}_k = \gamma_D^- \mathcal{V}_k = V_k,$$

for the exterior and interior traces and the single-layer boundary operator writes

$$(V_k \mu)(\mathbf{x}) := \int_{\Gamma} g_k(\mathbf{x}, \mathbf{y}) \psi(\mathbf{y}) dS_{\mathbf{y}}, \quad \text{for } \mu \in H^{-\frac{1}{2}}(\Gamma) \text{ and } \mathbf{x} \in \Gamma.$$

2.3. Relation between the Krein spectral shift function and the single-layer boundary operator

By [11], the Krein spectral shift function is defined as

$$\xi(k) = \frac{1}{2\pi i} \log \left(\frac{\det(S(k))}{\det(S_{1,k}) \cdots \det(S_{N,k})} \right),$$

where $S_{i,n}$ is the scattering matrix associated with the n th scatterer. These scattering matrices can be constructed $S_{i,n} = I + T_{i,n}$, where I is the identity matrix and $T_{i,n}$ is the T -matrix and the method of computing the T -matrix is fully discussed in [13] and [14].

The following theorem links the single-layer boundary operator with the Krein spectral shift function which inspires us to computing the Casimir energy via the scattering matrix or integral operator.

Theorem 1. [11] *Consider Ω as a domain assembling from individual objects Ω_i . Let V_k be the single-layer boundary operator defined on the boundary $\partial\Omega = \bigcup_{i=1}^N \partial\Omega_i$, and \tilde{V}_k is the “diagonal part” of V_k by restricting the integral kernel to the subset $\bigcup_{i=1}^N \partial\Omega_i \times \partial\Omega_i \subset \partial\Omega \times \partial\Omega$ then the operator $V_k \tilde{V}_k^{-1}$ is trace-class and*

$$\Xi(k) = \log \det \left(V_k \tilde{V}_k^{-1} \right).$$

Then for $k > 0$, we have

$$-\frac{1}{\pi} \text{Im} \Xi(k) = \frac{i}{2\pi} (\Xi(k) - \Xi(-k)) = \xi(k)$$

and by choosing $f(x) = x$ in (4), this gives the formula

$$\text{Tr} \left(\Delta^{\frac{1}{2}} + (N-1)\Delta_0^{\frac{1}{2}} - \sum_{i=1}^N \Delta_j^{\frac{1}{2}} \right) = \int_0^\infty \xi(k) dk = -\frac{1}{\pi} \int_0^\infty \Xi(ik) dk. \quad (7)$$

The equation (7) is used to compute the Casimir energy between the objects and the formula is written as

$$\mathcal{E} = \frac{\hbar c}{2} \int_0^\infty \xi(k) dk = -\frac{\hbar c}{2\pi} \int_0^\infty \Xi(ik) dk \quad (8)$$

Remark 1. Note that the integral $\frac{\hbar c}{2} \int_0^\infty \xi(k) dk$ in (8) is not Lebesgue convergence but might be Riemann integrable. Therefore, one should compute Casimir energy via the integral operator method but not the scattering matrix method.

2.4. Galerkin discretization and boundary element spaces

In order to compute the integral (8), we need to compute the log determinant of the operators $V_k \tilde{V}_k^{-1}$. In our numerical framework, we would like to use the Galerkin discretization to express the operators in matrix form and in this part, the explicit form of the element inside the matrix will be given and the Corresponding basis functions will be introduced as well.

Recall the domain of the single-layer boundary operator is $H^{-\frac{1}{2}}(\Gamma)$. To discretize this Sobolev space, we would like to introduce the triangulation \mathcal{T}_h of the boundary surface Γ with triangular surface elements τ_l and associated nodes \mathbf{x}_i s.t. $\overline{\mathcal{T}}_h = \bigcup_l \overline{\tau}_l$, where h is the mesh size and define the space of the continuous piecewise linear functions

$$P_h^1(\Gamma) = \{v_h \in C^0(\Gamma) : v_h|_{\tau_l} \in \mathbb{P}_1(\tau_l), \text{ for } \tau_l \in \mathcal{T}_h\},$$

where $\mathbb{P}_1(\tau_l)$ denotes the space of polynomials of order less than or equal to 1 on τ_l and typically, we use the following $P_h^1(\Gamma)$ space to discretize $H^{-\frac{1}{2}}(\Gamma)$:

$$P_h^1(\Gamma) := \text{span}\{\phi_j\} \subset H^{-\frac{1}{2}}(\Gamma)$$

with

$$\phi_j(\mathbf{x}_i) = \begin{cases} 1, & i = j, \\ 0, & i \neq j. \end{cases}$$

Having defined the basis function $P_h^1(\Gamma)$, we can represent each element inside the Galerkin discretization form. Assume there are N objects, then the matrix of the operator V_k is an N by N block matrix, written as

$$\mathbf{V}_k = \mathbf{V}(k) = \begin{bmatrix} \mathbf{V}_{11}(k) & \mathbf{V}_{12}(k) & \cdots & \mathbf{V}_{1N}(k) \\ \mathbf{V}_{21}(k) & \mathbf{V}_{22}(k) & \cdots & \mathbf{V}_{2N}(k) \\ \vdots & \vdots & \ddots & \vdots \\ \mathbf{V}_{N1}(k) & \mathbf{V}_{N2}(k) & \cdots & \mathbf{V}_{NN}(k) \end{bmatrix} \quad (9)$$

and the matrix $\tilde{\mathbf{V}}_k$ is the diagonal part of \mathbf{V}_k :

$$\tilde{\mathbf{V}}_k = \tilde{\mathbf{V}}(k) = \begin{bmatrix} \mathbf{V}_{11}(k) & 0 & \cdots & 0 \\ 0 & \mathbf{V}_{22}(k) & \cdots & 0 \\ \vdots & \vdots & \ddots & \vdots \\ 0 & 0 & \cdots & \mathbf{V}_{NN}(k) \end{bmatrix}. \quad (10)$$

Therefore, the element in the m th row and n th column of the block matrix $\mathbf{V}_{ij}(k)$ is

$$\mathbf{V}_{ij}^{(m,n)}(k) = \langle V_{ij}(k)\phi_m^{(i)}, \phi_n^{(j)} \rangle = \int_{\Gamma} \overline{\phi_n^{(j)}}(\mathbf{x}) \int_{\Gamma} g_k(\mathbf{x}, \mathbf{y}) \phi_m^{(i)}(\mathbf{y}) dS_{\mathbf{y}} dS_{\mathbf{x}}, \quad (11)$$

where $\phi^{(i)} = [\phi_1^{(i)} \quad \phi_2^{(i)} \quad \cdots \quad \phi_N^{(i)}]$ is the set of basis functions defined on the i th object and

$$\langle f, g \rangle = \int_{\Gamma} \overline{f(\mathbf{x})} g(\mathbf{x}) dS_{\mathbf{x}}$$

denotes the standard $L^2(\Gamma)$ inner product.

By (11), the explicit form of each element in matrix \mathbf{V}_k and $\tilde{\mathbf{V}}_k$ is known, therefore, the value of $\Xi(ik) = \log \det(V_{ik} \tilde{V}_{ik}^{-1})$ can be evaluated by computing $\log \frac{\det \mathbf{V}_{ik}}{\det \tilde{\mathbf{V}}_{ik}}$ with different values of k , which is the integrand of the Casimir formula (8). However, by plotting the value of this integrand with respect to different values of ik , we found that this function is exponentially decays with increasing the imaginary wavenumber ik (see Figure 1 (Left)) and shares the same trend with e^{-2Zk} , where Z is the minimal distance between two objects. This result is proved and summarized in the following theorem.

Theorem 2. *Let \mathbf{V}_{ik} and $\tilde{\mathbf{V}}_{ik}$ be the positive definite block matrices defined in (9) and (10) and they are partitioned as 2 by 2 block matrices*

$$\mathbf{V}_{ik} = \begin{bmatrix} \mathbb{V}_{11}(ik) & \mathbb{V}_{12}(ik) \\ \mathbb{V}_{21}(ik) & \mathbb{V}_{22}(ik) \end{bmatrix} \quad \text{and} \quad \tilde{\mathbf{V}}_{ik} = \begin{bmatrix} \mathbb{V}_{11}(ik) & 0 \\ 0 & \mathbb{V}_{22}(ik) \end{bmatrix}.$$

Denote $\{\lambda_i\}_i$ and $\{\tilde{\lambda}_i\}_i$ as the eigenvalues of them, separately and Z be the minimal distance between the objects. Then,

$$\|\mathbf{V}_{ik} - \tilde{\mathbf{V}}_{ik}\|_2 = \mathcal{O}(e^{-Zk})$$

and the integrand in (8) satisfies

$$\log \frac{\det \mathbf{V}_{ik}}{\det \tilde{\mathbf{V}}_{ik}} = \frac{\mathcal{O}(e^{-2Zk})}{\tilde{\lambda}_{\min} \text{gap}_{\min}}, \quad (12)$$

where $\tilde{\lambda}_{\min} = \min_i \tilde{\lambda}_i$ and $\text{gap}_{\min} = \min_i \text{gap}_i$ with gap_i defined as

$$\text{gap}_i := \begin{cases} \min_{\tilde{\lambda}_j \in \mathbb{V}_{22}} |\tilde{\lambda}_i - \tilde{\lambda}_j|, & \text{if } \tilde{\lambda}_i \in \lambda(\mathbb{V}_{11}) \\ \min_{\tilde{\lambda}_j \in \mathbb{V}_{11}} |\tilde{\lambda}_i - \tilde{\lambda}_j|, & \text{if } \tilde{\lambda}_i \in \lambda(\mathbb{V}_{22}). \end{cases}$$

Proof. By setting $E_{ik} = \mathbb{V}_{ik} - \tilde{\mathbb{V}}_{ik}$, we have

$$\|E_{ik}\|_2 = \left\| \begin{bmatrix} 0 & \mathbb{V}_{12}(ik) \\ \mathbb{V}_{21}(ik) & 0 \end{bmatrix} \right\|_2.$$

Since the elements in $\mathbb{V}_{12}(ik)$ and $\mathbb{V}_{21}(ik)$ are constructed by (11) which includes the Green's function g_{ik} (6), we can conclude $\|E_{ik}\|_2 = \mathcal{O}(e^{-Zk})$, where Z is the minimal distance between the objects.

To prove (12), we firstly assume the eigenvalues of the matrices \mathbb{V}_{ik} and $\tilde{\mathbb{V}}_{ik}$ are $\{\lambda_i\}_i$ and $\{\tilde{\lambda}_i\}_i$, respectively. Then, according to [15, Theorem 1], since E_{ik} and $\tilde{\mathbb{V}}_{ik}$ are symmetric matrices, we have the eigenvalue perturbation bound

$$|\lambda_i - \tilde{\lambda}_i| \leq \frac{\|E_{ik}\|_2^2}{\text{gap}_i}, \quad (13)$$

where

$$\text{gap}_i := \begin{cases} \min_{\tilde{\lambda}_j \in \mathbb{V}_{22}} |\lambda_i - \tilde{\lambda}_j|, & \text{if } \tilde{\lambda}_i \in \lambda(\mathbb{V}_{11}) \\ \min_{\tilde{\lambda}_j \in \mathbb{V}_{11}} |\lambda_i - \tilde{\lambda}_j|, & \text{if } \tilde{\lambda}_i \in \lambda(\mathbb{V}_{22}). \end{cases}$$

Since $\|E_{ik}\|_2 = \mathcal{O}(e^{-Zk})$, (13) becomes $\lambda_i - \tilde{\lambda}_i = \frac{\mathcal{O}(e^{-2Zk})}{\text{gap}_i}$. By setting $\tilde{\lambda}_{\min} = \min_i \tilde{\lambda}_i$ and $\text{gap}_{\min} = \min_i \text{gap}_i$, we have

$$\begin{aligned} \log \frac{\det \mathbb{V}_{ik}}{\det \tilde{\mathbb{V}}_{ik}} &= \sum_i \log \frac{\lambda_i}{\tilde{\lambda}_i} \\ &= \sum_i \log \left[1 + \frac{\mathcal{O}(e^{-2Zk})}{\tilde{\lambda}_i \text{gap}_i} \right] \\ &= \sum_i \frac{\mathcal{O}(e^{-2Zk})}{\tilde{\lambda}_i \text{gap}_i} + \text{h.o.t} \\ &\leq \sum_i \frac{\mathcal{O}(e^{-2Zk})}{\tilde{\lambda}_{\min} \text{gap}_{\min}} + \text{h.o.t} \\ &= \frac{\mathcal{O}(e^{-2Zk})}{\tilde{\lambda}_{\min} \text{gap}_{\min}} \end{aligned}$$

□

Note that the numerical experiments indicate that the eigenvalues $\{\tilde{\lambda}_i\}_i$ and the eigenvalue gaps $\{\text{gap}_i\}_i$ do not exponentially depend on k .

The integrand value of Casimir integral formula

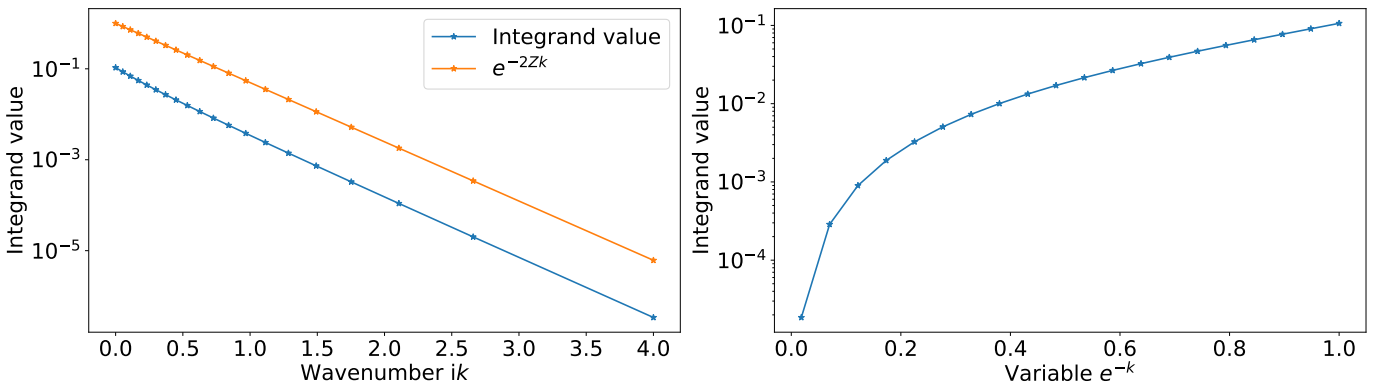


Figure 1: (Left) The integrand of the Casimir energy whose value exponentially decays with increasing imaginary wavenumber ik . The integrand function shares the same trend with e^{-2Zk} , where Z is the minimal distance between two objects. The scatterers are two spheres with equal radii $R = 1$ with minimal distance $Z = 1.5$. (Right) The integrand of the Casimir energy after changing the variable for applying the trapezoid quadrature rule.

Finally, one can apply the normal trapezoidal rule to calculate the integral $\int_0^\infty \Xi(ik)dk = \int_0^\infty \log \frac{\det \mathbf{V}_{ik}}{\det \tilde{\mathbf{V}}_{ik}} dk$ with variable changed. The steps are sketched as follows.

- Set $f(k) = \log \frac{\det \mathbf{V}_{ik}}{\det \tilde{\mathbf{V}}_{ik}}$ and the range of k is from 0 to ∞ .
- Let $k = -\log(y)$, then the integral $\int_0^\infty \log \frac{\det \mathbf{V}_{ik}}{\det \tilde{\mathbf{V}}_{ik}} dk$ becomes $\int_0^1 f(k)dk = \int_0^1 \frac{f(-\log(y))}{y} dy$.
- Set the range of k as (lb, ub) ² and the corresponding range for y is $(e^{-\text{ub}}, e^{-\text{lb}}) \subset [0, 1]$.
- Choose m quadrature points from the interval $(e^{-\text{ub}}, e^{-\text{lb}})$ and use the trapezoidal rule to evaluate the integral $\int_{e^{-\text{ub}}}^{e^{-\text{lb}}} \frac{f(-\log(y))}{y} dy$. Figure 1 (Right) plots the integrand with regard to new variable $y (= e^{-k})$.

3. Spectral property of the integral operators

The matrix M_∞ is a compact perturbation of matrix M , which makes the eigenvalues of them close to each other. Therefore, if we plot the eigenvalues of the matrix MM_∞^{-1} , we can notice that there are many eigenvalues closed to 1 and nearly contributes nothing to the log determinant. This spectral property inspires us to use some iteration method to approximate the extreme eigenvalues of MM_∞^{-1} . In order to make the computation process more efficiently, we will introduce an inverse-free method to speed up this process which makes us deal with the large-scale problem in the future.

4. Efficient methods for computing $\log \det(\mathbf{V}_{ik}\tilde{\mathbf{V}}_{ik}^{-1})$

By Section 2, to compute the Casimir energy, it is necessary to evaluate the term $\log \frac{\det \mathbf{V}_{ik}}{\det \tilde{\mathbf{V}}_{ik}} = \log \det(\mathbf{V}_{ik}\tilde{\mathbf{V}}_{ik}^{-1})$ with different values of k . In this section, several efficient methods will be introduced to compute this log determinant.

The log determinant of the matrix $\mathbf{V}_{ik}\tilde{\mathbf{V}}_{ik}^{-1}$ is equal to the sum of the logarithm of the eigenvalues of $\mathbf{V}_{ik}\tilde{\mathbf{V}}_{ik}^{-1}$. Since $\tilde{\mathbf{V}}_{ik}$ is a compact perturbation of \mathbf{V}_{ik} , most of the eigenvalues are close to 1 (shown in the Figure 2), which almost contribute nothing on the value of Casimir energy. Therefore, the computation process for the large-scale problem can become efficient if only multiple extreme eigenvalues that mainly contribute to the log determinant are computed. In addition, we should also avoid directly computing the inverse of the matrix $\tilde{\mathbf{V}}_{ik}$ since the computational complexity is cubic with respect to the matrix dimension.

In what follows, one method called inverse-free Krylov subspace method will be introduced to computed multiple extreme eigenvalues. For each quadrature point $k_j, j = 1, \dots, N$, one can directly apply this method to find the log determinant of $\mathbf{V}_{ik_j}\tilde{\mathbf{V}}_{ik_j}^{-1}$. However, by recalling Figure 1, most of the quadrature points are closed to each other, which inspires us to recycle the subspace obtained from $\mathbf{V}_{ik_j}\tilde{\mathbf{V}}_{ik_j}^{-1}$ and use it for $\mathbf{V}_{ik_{j+1}}\tilde{\mathbf{V}}_{ik_{j+1}}^{-1}$. Afterwards, another efficient method based on LU decomposition for inverting the diagonal block matrix of $\tilde{\mathbf{V}}_{ik}$ and standard Arnoldi iterations will be demonstrated and its corresponding recycling-subspace-based method will be discussed. Finally, the comparison of the performance and the complexity of these methods on approximating the log determinant will be shown.

²“ub” is short for upperbound and “lb” is short for lowerbound.

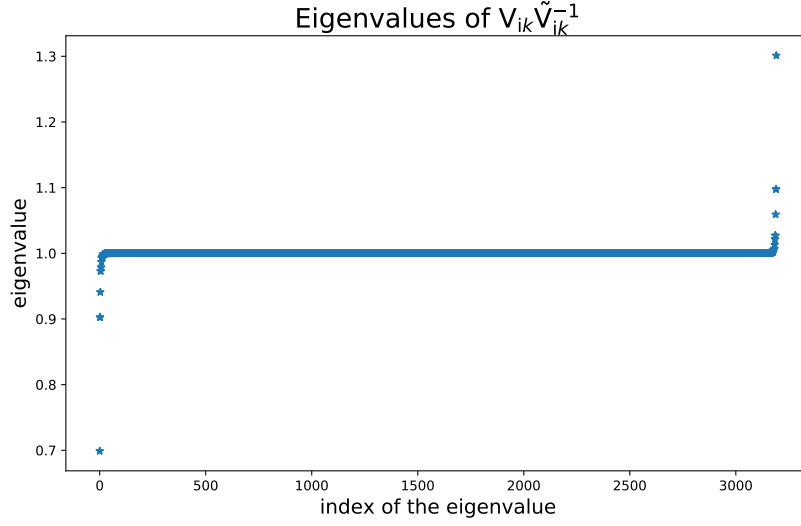


Figure 2: The eigenvalues of the matrix $V_{ik} \tilde{V}_{ik}^{-1}$ when $ik = 0.8i$. The scatterers are two spheres with equal radii $r_1 = r_2 = 1$ and the minimal distance between them is $Z = 0.5$.

4.1. Method I: Inverse-free Krylov subspace method

Consider the eigenvalue problem:

$$V_{ik} \tilde{V}_{ik}^{-1} \mathbf{x} = \lambda \mathbf{x}, \quad (14)$$

where λ is the eigenvalue and \mathbf{x} is the corresponding eigenvector. This eigenvalue problem is equivalent to the following generalized eigenvalue problem:

$$V_{ik} \tilde{\mathbf{x}} = \lambda \tilde{V}_{ik} \tilde{\mathbf{x}}. \quad (15)$$

Thus, we can focus on solving the problem (15) instead of (14) to avoid computing the matrix inversion. By [16][17], the authors proposed an inverse-free Krylov subspace method for computing a few extreme eigenvalues of the symmetric definite generalized eigenvalue problem and the following algorithm summarizes this method.

Algorithm 1: Inverse-free Krylov subspace method for computing multiple extreme eigenvalues of the generalized eigenvalue problem $A\mathbf{x} = \lambda B\mathbf{x}$

Input: Symmetric matrix $A \in \mathbb{R}^{n \times n}$, s.p.d matrix $B \in \mathbb{R}^{n \times n}$, an initial approximation \mathbf{x} with $\|\mathbf{x}\| = 1$, the shift $\rho = 1$ and the dimension of the Krylov subspace $m \geq 1$

Output: The approximated extreme eigenvalues of $A\mathbf{x} = \lambda B\mathbf{x}$

- 1: Construct a basis Z_m for the Krylov subspace $K_m = \text{span}(\mathbf{x}, (A - \rho B)\mathbf{x}, \dots, (A - \rho B)^{m-1}\mathbf{x})$ with dimension m
 - 2: Project A and B on Z : $A_m = Z_m^T (A - \rho B) Z_m$, $B_m = Z_m^T B Z_m$
 - 3: Compute all the eigenpairs $\{(\lambda_i, \mathbf{x}_i)\}_{i=1, \dots, m}$ for the matrix pencil (A_m, B_m)
 - 4: Add each eigenvalue in $\{\lambda_i\}_{i=1, \dots, m}$ with the shift $\rho = 1$: $\tilde{\lambda}_i = \lambda_i + 1$, for $i = 1, \dots, m$
-

Algorithm 1 can make us approximate m extreme eigenvalues for the matrix pencil (A, B) where m is the dimension of the Krylov subspace K_m in Step 1, Algorithm 1. Moreover, since most of the eigenvalues of $V_{ik} \tilde{V}_{ik}^{-1}$ are around 1, it is better to set the shift ρ as 1, otherwise, we need more iterations to make the eigenvalues approximate to the exact ones [16].

Therefore, for each quadrature point ik_j , for $j = 1, \dots, N$, we can apply Algorithm 1 to compute the eigenvalues $\{\lambda_i^{(j)}\}_{i=1, \dots, m}$ for $V_{ik_j} \tilde{V}_{ik_j}^{-1}$, then the value of $\log \det(V_{ik_j} \tilde{V}_{ik_j}^{-1})$ can be approximated by

$$\log \det(V_{ik_j} \tilde{V}_{ik_j}^{-1}) \approx \sum_{i=1}^m \log \left(\lambda_i^{(j)} \right), \quad j = 1, \dots, N.$$

In order to make this inverse-free method become more efficient, one can recycle the subspace obtained from the first wavenumber ik_1 case by extracting several eigenvectors associated with the extremal eigenvalues in Step 3, Algorithm 1 and recovering the eigenvectors for the matrix pair $(V_{ik_1}, \tilde{V}_{ik_1})$ by multiplying the basis Z_m in Step 1, Algorithm 1 with the extracted eigenvectors. After orthogonalizing the resulting vectors, they are recycled as a basis for the next wavenumber's case.

For the second wavenumber, we initially compute the approximated eigenvalues $(\{\tilde{\lambda}_i\})$ and eigenvectors $(\{\tilde{x}_i\})$ with the recycled subspace and use the residual vectors $\{r_i = V_{ik_2}\tilde{x}_2\} - \tilde{\lambda}_i\tilde{V}_{ik_1}\tilde{x}_i$ to expand the subspace. With the expanded subspace, we recompute the eigenpairs for the second wavenumber's case and extract the resulting eigenvectors for the third wavenumber and so on. This improved inverse-free Krylov subspace method

based on the recycled subspace is completely described in Algorithm 2.

Algorithm 2: Inverse-free recycled Krylov subspace method for sequences of generalized eigenvalue problems $A^{(i)}\mathbf{x} = \lambda B^{(i)}\mathbf{x}$

Input: N : the number of matrix pencils $(A^{(i)}, B^{(i)})$, an initial approximation \mathbf{x} with $\|\mathbf{x}\| = 1$, the shift $\rho = 1$, the dimension of Krylov subspace $m \geq 1$ and the number of chosen extreme eigenvalues $\{s_i\}_i$, for $i = 1, 2, \dots, (N-1)$

Output: The approximated extreme eigenvalues of $A\mathbf{x} = \lambda B\mathbf{x}$

1: When $i = 1$:

- (a) Compute the basis $Z_m^{(1)}$ for the Krylov subspace
 $K_m^{(1)} = \text{span}(\mathbf{x}, (A^{(1)} - \rho B^{(1)})\mathbf{x}, \dots, (A^{(1)} - \rho B^{(1)})^{m-1}\mathbf{x})$ with dimension m
- (b) Project $A^{(1)}$ and $B^{(1)}$ on $Z_m^{(1)}$: $A_m^{(1)} = Z_m^{(1)H}(A^{(1)} - \rho B^{(1)})Z_m^{(1)}$, $B_m^{(1)} = Z_m^{(1)H}B^{(1)}Z_m^{(1)}$
- (c) Compute the eigenvalues $\boldsymbol{\lambda}^{(1)} = \{\lambda_1^{(1)}, \dots, \lambda_m^{(1)}\}$ and eigenvectors $\mathbf{X}_m^{(1)} = [\mathbf{x}_1^{(1)}, \dots, \mathbf{x}_m^{(1)}]$ for $A_m^{(1)}\mathbf{x} = \lambda B_m^{(1)}\mathbf{x}$ and note that the approximated eigenvalues for $A^{(1)}\mathbf{x} = \lambda B^{(1)}\mathbf{x}$ are $\{\lambda_1^{(1)} + \rho, \dots, \lambda_m^{(1)} + \rho\}$
- (d) Extract s_1 eigenvectors from $\mathbf{X}_m^{(1)}$, which correspond to s_1 extreme eigenvalues and relabel them as $\mathbf{X}_{s_1}^{(1)} = [\mathbf{x}_1^{(1)}, \dots, \mathbf{x}_{s_1}^{(1)}]$
- (e) Recover the eigenvectors for $A^{(1)}\mathbf{x} = \lambda B^{(1)}\mathbf{x}$ by computing $Z_m^{(1)}\mathbf{X}_{s_1}^{(1)}$ and orthogonalize it to obtain the temporary basis $\tilde{Z}_{s_1}^{(2)} = \text{orth}(Z_m^{(1)}\mathbf{X}_{s_1}^{(1)})$ for the second matrix pencil $(A^{(2)}, B^{(2)})$

2: When $i = 2$:

- (a) Project $A^{(2)}$ and $B^{(2)}$ on $\tilde{Z}_{s_1}^{(2)}$: $\tilde{A}_{s_1}^{(2)} = \tilde{Z}_{s_1}^{(2)H}A^{(2)}\tilde{Z}_{s_1}^{(2)}$, $\tilde{B}_{s_1}^{(2)} = \tilde{Z}_{s_1}^{(2)H}B^{(2)}\tilde{Z}_{s_1}^{(2)}$
- (b) Compute the eigenvalues $\tilde{\boldsymbol{\lambda}}^{(2)} = \{\tilde{\lambda}_1^{(2)}, \dots, \tilde{\lambda}_{s_1}^{(2)}\}$ and eigenvectors $\tilde{\mathbf{X}}_{s_1}^{(2)} = [\tilde{\mathbf{x}}_1^{(2)}, \dots, \tilde{\mathbf{x}}_{s_1}^{(2)}]$ for $\tilde{A}_{s_1}^{(2)}\tilde{\mathbf{x}} = \lambda \tilde{B}_{s_1}^{(2)}\tilde{\mathbf{x}}$
- (c) Compute the residuals $\mathbf{r}_i^{(2)} = A^{(2)}\tilde{Z}_{s_1}^{(2)}\tilde{\mathbf{x}}_i^{(2)} - \tilde{\lambda}_i^{(2)}B^{(2)}\tilde{Z}_{s_1}^{(2)}\tilde{\mathbf{x}}_i^{(2)}$ for $i = 1, 2, \dots, s_1$ and denote $\mathbf{r}^{(2)} = [\mathbf{r}_1^{(2)}, \dots, \mathbf{r}_{s_1}^{(2)}]$
- (d) Construct the basis $Z_{2s_1}^{(2)}$ for $(A^{(2)}, B^{(2)})$ by extending the temporary basis $\tilde{Z}_{s_1}^{(2)}$ with the residues $\mathbf{r}^{(2)}$ and orthogonalizing the extended subspace: $Z_{2s_1}^{(2)} = [\tilde{Z}_{s_1}^{(2)}, \tilde{\mathbf{r}}^{(2)}]$, where $\tilde{\mathbf{r}}^{(2)} = \text{orth}(\mathbf{r}^{(2)})$
- (e) Project $A^{(2)}$ and $B^{(2)}$ on $Z_{2s_1}^{(2)}$:

$$A_{2s_1}^{(2)} = Z_{2s_1}^{(2)H}A^{(2)}Z_{2s_1}^{(2)} = \begin{bmatrix} \tilde{A}_{s_1}^{(2)} & \tilde{Z}_{s_1}^{(2)H}A^{(2)}\tilde{\mathbf{r}}^{(2)} \\ \tilde{\mathbf{r}}^{(2)H}A^{(2)}\tilde{Z}_{s_1}^{(2)} & \tilde{\mathbf{r}}^{(2)H}A^{(2)}\tilde{\mathbf{r}}^{(2)} \end{bmatrix},$$

$$B_{2s_1}^{(2)} = Z_{2s_1}^{(2)H}B^{(2)}Z_{2s_1}^{(2)} = \begin{bmatrix} \tilde{B}_{s_1}^{(2)} & \tilde{Z}_{s_1}^{(2)H}B^{(2)}\tilde{\mathbf{r}}^{(2)} \\ \tilde{\mathbf{r}}^{(2)H}B^{(2)}\tilde{Z}_{s_1}^{(2)} & \tilde{\mathbf{r}}^{(2)H}B^{(2)}\tilde{\mathbf{r}}^{(2)} \end{bmatrix}$$

- (f) Repeat Step 1(c)-(e) for these projected matrices to compute the approximated eigenvalues

$\boldsymbol{\lambda}^{(2)} = \{\lambda_1^{(2)}, \dots, \lambda_{2s_1}^{(2)}\}$ and eigenvectors $\mathbf{X}_{2s_1}^{(2)} = [\mathbf{x}_1^{(2)}, \dots, \mathbf{x}_{2s_1}^{(2)}]$ for $(A_{2s_1}^{(2)}, B_{2s_1}^{(2)})$ and obtain the temporary basis $\tilde{Z}_{s_2}^{(3)}$ for the third matrix pencil $(A^{(3)}, B^{(3)})$

- 3: For $i = 3, \dots, N$, repeat the Step 2 to compute the approximated eigenvalues $\boldsymbol{\lambda}^{(i)} = \{\lambda_1^{(i)}, \dots, \lambda_{2s_{i-1}}^{(i)}\}$ and eigenvectors $\mathbf{X}_{2s_{i-1}}^{(i)} = [\mathbf{x}_1^{(i)}, \dots, \mathbf{x}_{2s_{i-1}}^{(i)}]$ for each matrix pencil
-

In this case, the value of $\log \det(\mathbf{V}_{ik_j} \tilde{\mathbf{V}}_{ik_j}^{-1})$ can be approximated by

$$\log \det(\mathbf{V}_{ik_j} \tilde{\mathbf{V}}_{ik_j}^{-1}) \approx \begin{cases} \sum_{i=1}^m \log(\lambda_i^{(j)}) & j = 1 \\ \sum_{i=1}^{2s_{j-1}} \log(\lambda_i^{(j)}) & j = 2, \dots, N \end{cases} \quad (16)$$

4.2. Method II: Standard Arnoldi method

Another efficient approach for computing $\log \det(\mathbf{V}_{ik} \tilde{\mathbf{V}}_{ik}^{-1})$ is to initially find the inverse of $\tilde{\mathbf{V}}_{ik}$ by computing the LU decomposition for each diagonal block matrix and solving the linear system on each subdomain. Afterwards, by applying the standard Arnoldi iterations on $\mathbf{V}_{ik} \tilde{\mathbf{V}}_{ik}^{-1}$, we can obtain its the Hessenberg matrix, whose eigenvalues can be used to approximate the ones of $\mathbf{V}_{ik} \tilde{\mathbf{V}}_{ik}^{-1}$.

To be specific, the inverse of the matrix $\tilde{\mathbf{V}}_{ik}$ is

$$\tilde{\mathbf{V}}_{ik}^{-1} = \tilde{\mathbf{V}}(ik)^{-1} = \begin{bmatrix} \mathbf{V}_{11}(ik) & 0 & \cdots & 0 \\ 0 & \mathbf{V}_{22}(ik) & \cdots & 0 \\ \vdots & \vdots & \ddots & \vdots \\ 0 & 0 & \cdots & \mathbf{V}_{NN}(ik) \end{bmatrix}^{-1} = \begin{bmatrix} \mathbf{V}_{11}^{-1}(ik) & 0 & \cdots & 0 \\ 0 & \mathbf{V}_{22}^{-1}(ik) & \cdots & 0 \\ \vdots & \vdots & \ddots & \vdots \\ 0 & 0 & \cdots & \mathbf{V}_{NN}^{-1}(ik) \end{bmatrix}.$$

We can compute LU decomposition of each diagonal block matrix $\mathbf{V}_{ii} = \mathbf{V}_{ii}(ik)$ for $i = 1, 2, \dots, N$ and the decomposition is written as $\mathbf{V}_{ii} = \mathbf{L}_{ii} \mathbf{U}_{ii}$, where \mathbf{L}_{ii} and \mathbf{U}_{ii} are lower and upper triangular matrices, respectively. Afterwards, by solving the linear system $\mathbf{L}_{ii} \mathbf{U}_{ii} \mathbf{x}_j = \mathbf{e}_j$, for each $j = 1, 2, \dots, N_{\mathbf{V}_{ii}}$, where \mathbf{e}_j denotes the vector with a 1 in the j th coordinate and 0's elsewhere and $N_{\mathbf{V}_{ii}}$ is the dimension of the block \mathbf{V}_{ii} , we obtain the inverse of \mathbf{V}_{ii} with expression $\mathbf{V}_{ii}^{-1} = [\mathbf{x}_1 \ \cdots \ \mathbf{x}_{N_{\mathbf{V}_{ii}}}]$.

Denote the inverse of the matrix $\tilde{\mathbf{V}}_{ik}$ computed by the above inverse-free LU decomposition method as $\tilde{\mathbf{V}}_{ik}^{-1, \text{LU}}$. To approximate multiple extreme eigenvalues of $\mathbf{V}_{ik} \tilde{\mathbf{V}}_{ik}^{-1, \text{LU}}$, we would like to firstly construct the Krylov subspace $K_m(\mathbf{V}_{ik} \tilde{\mathbf{V}}_{ik}^{-1, \text{LU}}, \mathbf{b})$, where \mathbf{b} is some initial vector and m is the dimension of this Krylov subspace. Afterwards, we implement the standard Arnoldi iteration to obtain the orthogonal basis of this order- m Krylov subspace and project the matrix $\mathbf{V}_{ik} \tilde{\mathbf{V}}_{ik}^{-1, \text{LU}}$ onto this basis. This projection matrix is called the Hessenberg matrix and we denote it as H_m . By [18], the eigenvalues of H_m (which are also called Ritz eigenvalues) can give good approximations on extreme eigenvalues of $\mathbf{V}_{ik} \tilde{\mathbf{V}}_{ik}^{-1, \text{LU}}$. The following algorithm lists the general steps described above.

Algorithm 3: Standard Arnoldi method for computing multiple extreme eigenvalues of the eigenvalue problem $AB^{-1}\mathbf{x} = \mu\mathbf{x}$

Input: Block matrix $A \in \mathbb{R}^{n \times n}$, diagonal block matrix $B \in \mathbb{R}^{n \times n}$ and the dimension of the Krylov subspace $m \geq 1$

Output: The approximated extreme eigenvalue of $AB^{-1}\mathbf{x} = \mu\mathbf{x}$

- 1: Use LU decomposition to compute the inverse of each diagonal block matrix in B
 - 2: Use standard Arnoldi method to compute the Hessenberg matrix H_m of AB^{-1}
 - 3: Compute all the eigenpairs $\{(\mu_i, \mathbf{x}_i)\}_{i=1, \dots, m}$ of H_m
-

By denoting the the eigenvalues of H_m as $\{\mu_i\}_{i=1, \dots, m}$, the value of $\log \det(\mathbf{V}_{ik} \tilde{\mathbf{V}}_{ik}^{-1})$ can be approximated by

$$\log \det(\mathbf{V}_{ik} \tilde{\mathbf{V}}_{ik}^{-1}) \approx \sum_{i=1}^m \log(\mu_i).$$

Same with the inverse-free Krylov subspace method, one can also recycle the eigenvectors associated with the extreme eigenvalues from the initial subspace for the first wavenumber, expand it with some vectos (In

Algorithm 2, they are residual vectors) and use the complemented basis for the second wavenumber's case. Algorithm 4 summarizes the whole steps for this recycling process.

Algorithm 4: Standard Arnoldi methods with recycled subspaces for sequences of eigenvalue problems

$$A^{(i)} (B^{(i)})^{-1} \mathbf{x} = \mu \mathbf{x}$$

Input: N : the number of matrices $A^{(i)} (B^{(i)})^{-1}$, where $A^{(i)}$ are block matrices and $B^{(i)}$ are diagonal block matrices, an initial approximation x with $\|x\| = 1$, the shift $\rho = 1$, the dimension of Krylov subspace $m \geq 1$ and the number of chosen extreme eigenvalues $\{s_i\}_i$, for $i = 1, 2, \dots, (N - 1)$

1: When $i = 1$:

- (a) Use LU decomposition to compute the inverse of each diagonal block matrix in $B^{(1)}$
- (b) Apply the standard Arnoldi method to compute the Arnoldi vectors $Z_m^{(1)}$ and Hessenberg matrix $H_m^{(1)}$ for $A^{(1)} (B^{(1)})^{-1}$, which satisfy $H_m^{(1)} = Z_m^{(1)H} (A^{(1)} (B^{(1)})^{-1}) Z_m^{(1)}$
- (c) Compute the eigenvalues $\mu^{(1)} = \{\mu_1^{(1)}, \dots, \mu_m^{(1)}\}$ and eigenvectors $\mathbf{X}_m^{(1)} = [\mathbf{x}_1^{(1)}, \dots, \mathbf{x}_m^{(1)}]$ for $H_m^{(1)}$
- (d) Extract s_1 eigenvectors from $\mathbf{X}_m^{(1)}$, which correspond to s_1 extreme eigenvalues and relabel them as $\mathbf{X}_{s_1}^{(1)} = [\mathbf{x}_1^{(1)}, \dots, \mathbf{x}_{s_1}^{(1)}]$
- (e) Recover the eigenvectors for $A^{(1)} (B^{(1)})^{-1} x = \mu x$ by computing $Z_m^{(1)} \mathbf{X}_{s_1}^{(1)}$ and orthogonalize it to obtain the temporary basis $\tilde{Z}_{s_1}^{(2)} = \text{orth} (Z_m^{(1)} \mathbf{X}_{s_1}^{(1)})$ for the second eigenvalue problem $A^{(2)} (B^{(2)})^{-1} \mathbf{x} = \lambda \mathbf{x}$

2: When $i = 2$:

- (a) Repeat Step 1(a) on $B^{(2)}$ and project $A^{(2)} (B^{(2)})^{-1}$ on $\tilde{Z}_{s_1}^{(2)}$:

$$\tilde{H}_{s_1}^{(2)} = \tilde{Z}_{s_1}^{(2)H} (A^{(2)} (B^{(2)})^{-1}) \tilde{Z}_{s_1}^{(2)}$$

- (b) Compute the eigenvalues $\tilde{\mu}^{(2)} = \{\tilde{\mu}_1^{(2)}, \dots, \tilde{\mu}_{s_1}^{(2)}\}$ and eigenvectors $\tilde{\mathbf{X}}_{s_1}^{(2)} = [\tilde{\mathbf{x}}_1^{(2)}, \dots, \tilde{\mathbf{x}}_{s_1}^{(2)}]$ for $A^{(2)} (B^{(2)})^{-1} x = \lambda x$
- (c) Compute the residuals $r_i^{(2)} = (A^{(2)} (B^{(2)})^{-1}) \tilde{Z}_{s_1}^{(2)} \tilde{\mathbf{x}}_i^{(2)} - \tilde{\mu}_i^{(2)} \tilde{Z}_{s_1}^{(2)} \tilde{\mathbf{x}}_i^{(2)}$, for $i = 1, 2, \dots, s_1$ and denote $\mathbf{r}^{(2)} = [\mathbf{r}_1^{(2)}, \dots, \mathbf{r}_{s_1}^{(2)}]$
- (d) Construct the basis $Z_{2s_1}^{(2)}$ for $A^{(2)} (B^{(2)})^{-1}$ by extending the temporary basis $\tilde{Z}_{s_1}^{(2)}$ with the residues $\mathbf{r}^{(2)}$ and orthogonalizing the extended subspace: $Z_{2s_1}^{(2)} = [\tilde{Z}_{s_1}^{(2)}, \tilde{\mathbf{r}}^{(2)}]$, where $\tilde{\mathbf{r}}^{(2)} = \text{orth} (\mathbf{r}^{(2)})$
- (e) Project $A^{(2)} (B^{(2)})^{-1}$ on $Z_{2s_1}^{(2)}$:

$$H_{2s_1}^{(2)} = Z_{2s_1}^{(2)H} (A^{(2)} (B^{(2)})^{-1}) Z_{2s_1}^{(2)} = \begin{bmatrix} \tilde{H}_{s_1}^{(2)} & \tilde{Z}_{s_1}^{(2)H} (A^{(2)} (B^{(2)})^{-1}) \tilde{\mathbf{r}}^{(2)} \\ \tilde{\mathbf{r}}^{(2)H} (A^{(2)} (B^{(2)})^{-1}) \tilde{Z}_{s_1}^{(2)} & \tilde{\mathbf{r}}^{(2)H} (A^{(2)} (B^{(2)})^{-1}) \tilde{\mathbf{r}}^{(2)} \end{bmatrix}$$

- (f) Repeat Step 1(c)-(e) for the projected matrix $H_{2s_1}^{(2)}$ to compute the approximated eigenvalues $\mu^{(2)} = \{\mu_1^{(2)}, \dots, \mu_{2s_1}^{(2)}\}$ and eigenvectors $\mathbf{X}_{2s_1}^{(2)} = [\mathbf{x}_1^{(2)}, \dots, \mathbf{x}_{2s_1}^{(2)}]$ and obtain the temporary basis $\tilde{Z}_{s_2}^{(3)}$ for the third eigenvalue problem $A^{(3)} (B^{(3)})^{-1} x = \lambda x$

3: For $i = 3, \dots, N$, repeat the Step 2 to compute the approximated eigenvalues $\mu^{(i)} = \{\mu_1^{(i)}, \dots, \mu_{2s_{i-1}}^{(i)}\}$ and eigenvectors $\mathbf{X}_{2s_{i-1}}^{(i)} = [\mathbf{x}_1^{(i)}, \dots, \mathbf{x}_{2s_{i-1}}^{(i)}]$ for each eigenvalue problem

With Algorithm 4, the value of $\log \det(\mathbf{V}_{ik_j} \tilde{\mathbf{V}}_{ik_j}^{-1})$ can be approximated by

$$\log \det(\mathbf{V}_{ik_j} \tilde{\mathbf{V}}_{ik_j}^{-1}) \approx \begin{cases} \sum_{i=1}^m \log(\mu_i^{(j)}) & j = 1 \\ \sum_{i=1}^{2s_{j-1}} \log(\mu_i^{(j)}) & j = 2, \dots, N \end{cases} \quad (17)$$

4.3. Comparison between inverse-free Krylov subspace and standard Arnoldi method with or without recycling subspaces

In this part, the performances on approximating the $\log \det \mathbf{V}_{ik} \tilde{\mathbf{V}}_{ik}^{-1}$ and the complexity of Algorithm 1-4 will be compared. Consider two spheres with equal radii $r_1 = r_2 = 1$ and the minimal distance between them is denoted as Z , which is set as 0.5, 1.5 and 3.0. The dimension of the Krylov subspace m in Algorithm 1, Algorithm 3, Step 1(a), Algorithm 2 and Step 1(b), Algorithm 4 is $m = 100$.

Figure 3 plots the relative error of computing $\log \det \mathbf{V}_{ik} \tilde{\mathbf{V}}_{ik}^{-1}$ with inverse-free Krylov subspace method and standard Arnoldi method with or without recycling the subspace. For inverse-free Krylov subspace method, recycling the subspace increases the performance on approximating the log determinant and for the standard Arnoldi method, the relative error is not always improved with the subspace recycled. (change/add explanations)

Relative error of $\log \det \mathbf{V}_{ik} \tilde{\mathbf{V}}_{ik}^{-1}$ computed by inverse-free and standard Arnoldi methods with/without recycling subspaces

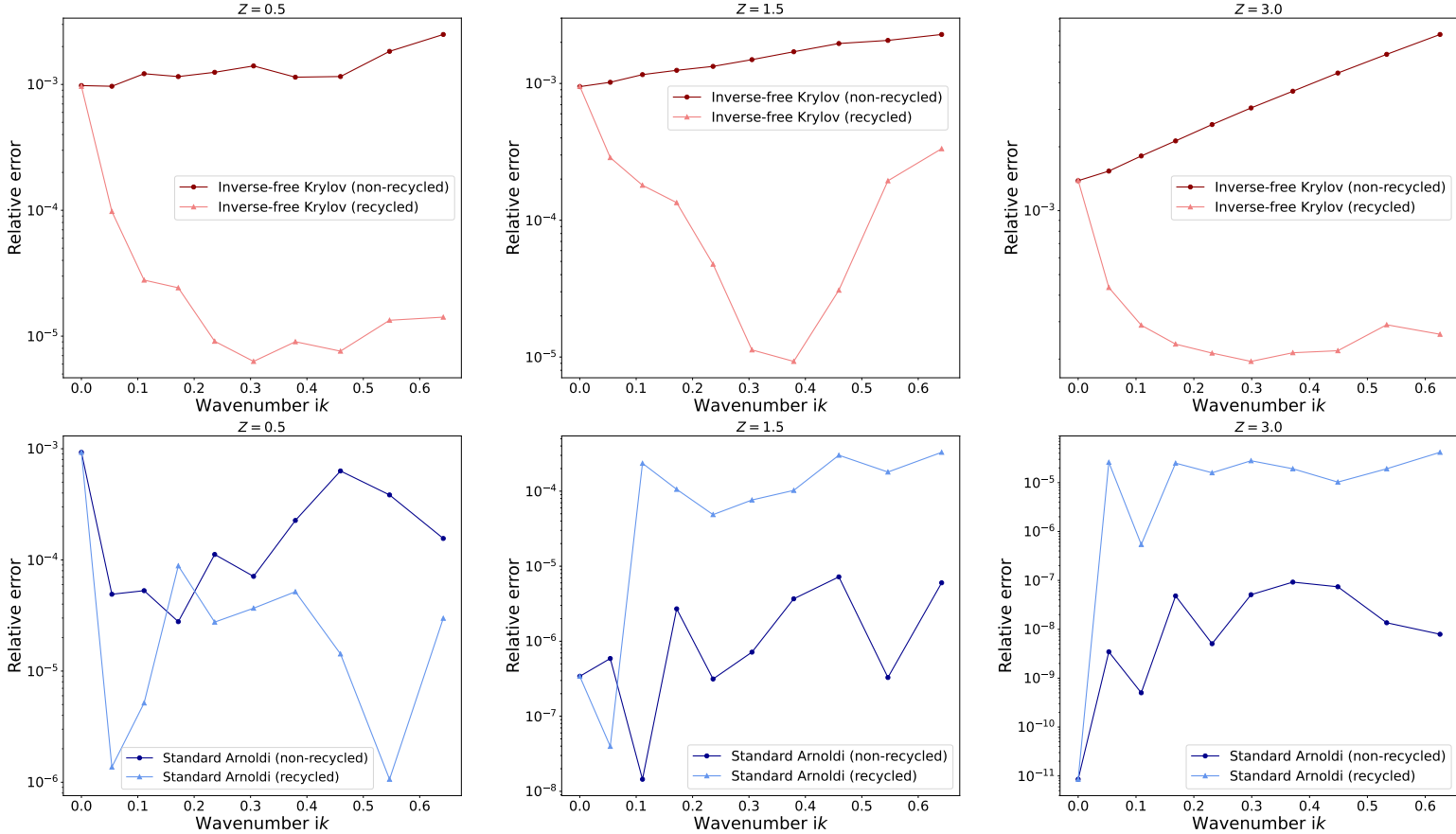


Figure 3: Relative error of $\log \det \mathbf{V}_{ik} \tilde{\mathbf{V}}_{ik}^{-1}$ computed by inverse-free Krylov subspace method and standard Arnoldi method with or without recycling subspaces.

In order to decide which method would be used to efficiently compute the Casimir energy, we explore the number of matrix-vector multiplications for these methods and they are list inside Table 1. (add graphs for comparing the number of matvec in four algorithms and add explanations)

Inverse-free Krylov subspace method		Standard Arnoldi method	
Without recycling	With recycling	Without recycling	With recycling
$(2m - 1)N$	$(2m - 1) + \sum_{i=1}^{N-1} s_i^2 + 4 \sum_{i=1}^{N-1} s_i$	$(m - 1)N$	$(m - 1) + \sum_{i=1}^{N-1} s_i^2 + 4 \sum_{i=1}^{N-1} s_i$

Table 1: The number of matrix-vector multiplications inside the inverse-free Krylov subspace and standard Arnoldi methods with or without recycling subspaces. N is the number of wavenumbers, m is the dimension of the Krylov subspace for the first wavenumber (in recycling case); for all the wavenumbers (in non-recycling case), n denotes the dimension of the matrices generated from the boundary operator discretizations and s_i is the number of the extracted eigenvectors for the i th wavenumber's case (in recycling case).

5. Numerical experiments

In this section, we are going to show the numerical results for computing the Casimir energy between two perfectly conducting objects, which are spheres, menger sponges, ice crystals and ellipsoids. The reference value of the Casimir energy is computed by the Richardson extrapolation method which is often used for obtaining the higher-order estimate at zero grid spacing. Denote $\mathcal{E}_{\text{fine}}$ and $\mathcal{E}_{\text{coarse}}$ as the Casimir energy numerically computed from the formula (8) by setting the grid size h as h_{fine} and h_{coarse} ($h_{\text{fine}} < h_{\text{coarse}}$), separately. Then, the high-accuracy result $\mathcal{E}_{\text{extrapolation}}$ can be generated from the following formula:

$$\mathcal{E}_{\text{extrapolation}} \approx \frac{h_{\text{coarse}}^2 \mathcal{E}_{\text{fine}} - h_{\text{fine}}^2 \mathcal{E}_{\text{coarse}}}{h_{\text{coarse}}^2 - h_{\text{fine}}^2}. \quad (18)$$

In addition, the asymptotic series of the Casimir energy with large separation between scatterers are also available in two spheres' case and the series can be found in [8] for both equal and unequal radii's cases.

5.1. Two spheres case

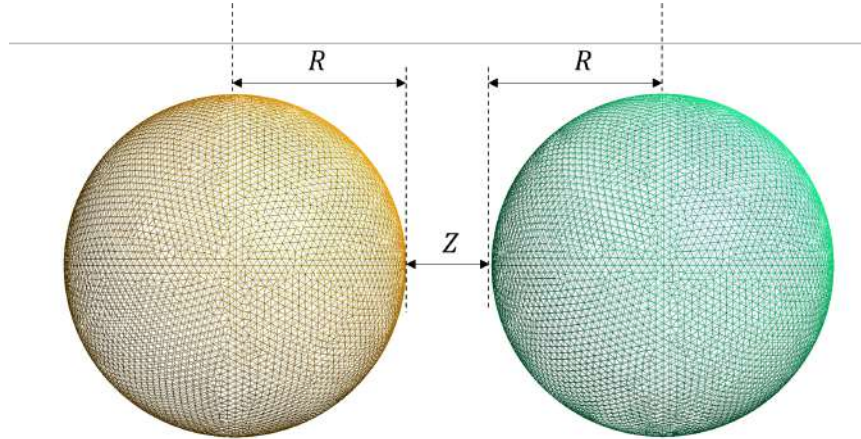


Figure 4: Two spheres with equal radii: R represents the radius of the spheres and Z is the distance between them.

Consider two perfectly conducting spheres with equal radii R in Figure 4. By denoting the distance between them as Z , the asymptotic expression of the integrand of the Casimir integral formula (8) introduced in [19] is written as:

$$\Xi(k) = -\frac{R_1 R_2}{4Z(R_1 + R_2 + Z)} e^{2iZk} + o(e^{-2Z\text{Im}k}), \quad (19)$$

where R_1 and R_2 are the radius of the spheres.

Figure 5 plots the quotient of the leading term in (19) and the estimated integrand value on different wavenumbers ik . This quotient provides with a good estimate on the upperbound of the integration of the Casimir energy formula (8). For example, when the distance $Z = 1.5$, if k in wavenumber ik is larger than 7, the quotient gets far away from 1, which means the approximated integrand value is not close to the asymptotic term and $7i$ is chosen as the upperbound when $Z = 1.5$. The following table lists the upperbound of the integration for the distance Z varying from 0.5 to 3.0.

Distance Z	0.5	0.75	1.0	1.25	1.5	1.75	2.0	2.25	2.5	2.75	3.0
Upperbound	24i	17i	13i	9i	7i	6i	6i	5i	5i	4i	4i

Table 2: The estimated upperbound for the Casimir energy formula for different minimal distance Z varying from 0.5 to 3.0.

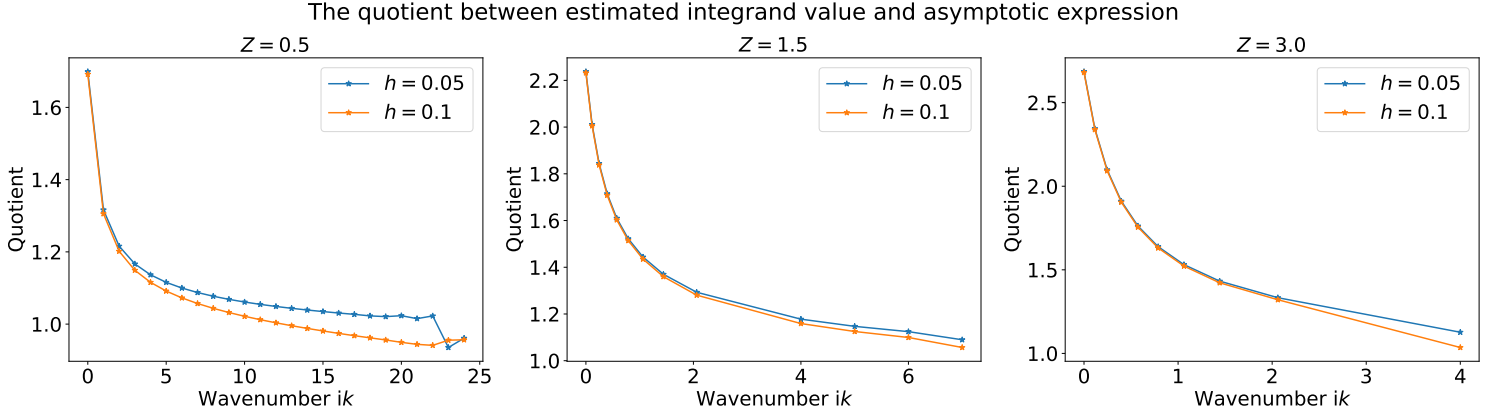


Figure 5: The quotient of the leading term of the series (19) and the estimated integrand value along the imaginary axis with grid size h set as $h_{\text{coarse}} = 0.1$ and $h_{\text{fine}} = 0.05$ in two spheres with equal radii's case. The radius of the spheres is $R = 1$ and the minimal distance between them is $Z = 0.5, 1.5$ and 3.0 .

Remark 2 (Determine the upperbound of the integration from the error tolerance). By Figure 1, since the integrand value $\log \det \mathbf{V}_{ik} \tilde{\mathbf{V}}_{ik}^{-1}$ shares the same trend with e^{-2Zk} in (8), one can apply the function $f(k) = Ce^{-2Zk}$ to fit the curve of the estimated integrand values. With the coefficient C determined, one can estimate the absolute error for approximating the Casimir integral by computing:

$$\epsilon \approx \int_{\kappa}^{\infty} f(k) dk = \frac{Ce^{-2Z\kappa}}{2Z},$$

where κ is the upperbound of the integration. Meanwhile, one can also determine the upperbound of the integration with regard to different error tolerance.

For example, if one aims to have at least three significant digits of the exact value of the Casimir integral, the upperbound can be set as the following table lists:

Distance Z	0.5	0.75	1.0	1.25	1.5	1.75	2.0	2.25	2.5	2.75	3.0
Upperbound	10i	7i	5i	5i	4i	3i	3i	2i	2i	2i	2i

Table 3: The estimated upperbound for the Casimir energy formula for different minimal distance Z varying from 0.5 to 3.0.

With the upperbound of the integration determined, one can start to estimate the Casimir energy between two spheres with radius $R = 1$ at the distance of Z via the formula (8) in two different refinement levels: $h_{\text{fine}} = 0.05$ ($\dim(\mathbf{V}_{ik}) = 12603$) and $h_{\text{coarse}} = 0.1$ ($\dim(\mathbf{V}_{ik}) = 3192$).

Afterwards, the extrapolation result can be obtained by substituting these Casimir energy estimates into

the formula (18). This result would be regarded as the extrapolation value of the Casimir energy, which would be used to compare with the estimates derived from the asymptotic series introduced below.

According to [8], the Casimir energy between two spheres (with equal radii R) at asymptotically large separations can be obtained as a series in terms of the ratio of centre distance L ($L = 2R + Z$) to sphere radius R :

$$\mathcal{E} = -\frac{\hbar c}{\pi} \frac{1}{L} \sum_{n=0}^{\infty} b_n \left(\frac{R}{L}\right)^{n+2}, \quad (20)$$

where the first six coefficients are $b_0 = -1/4$, $b_1 = -1/4$, $b_2 = -77/48$, $b_3 = -25/16$, $b_4 = -29837/2880$, $b_5 = -6491/1152$. Figure 6 shows the comparison between the Casimir energy computed from asymptotic series (20) and the exact value evaluated through Richardson extrapolation. Here, we observe that the asymptotic value gradually approaches to the exact value as the distance Z increases since the asymptotic expansion (20) only works when the distance between two spheres is asymptotically large.

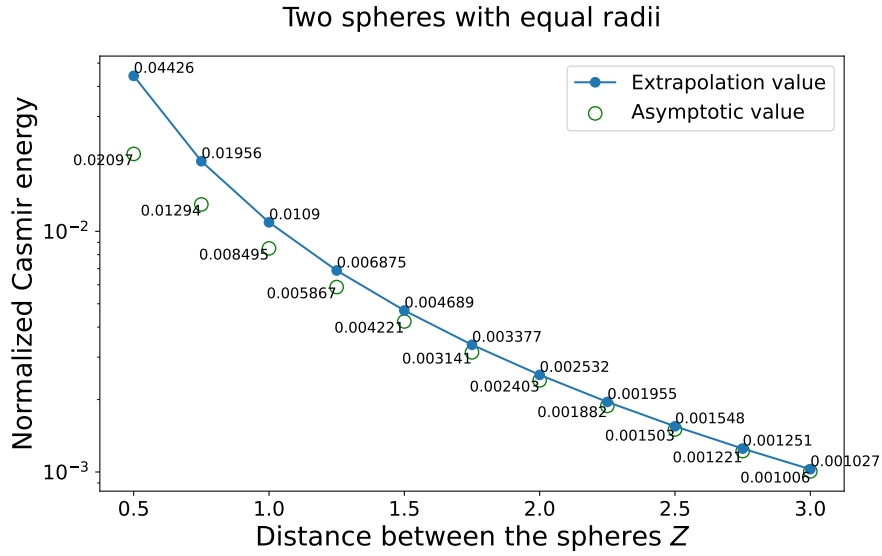


Figure 6: Normalized Casimir energy³ in two spheres with equal radii's case. The radius is $R = 1$ and the distance Z ranges from 0.5 to 3.0. The exact value of the (normalized) Casimir energy has been written beside the data point, which is round up to 4 significant digits.

Figure 7 shows the relative distance between the estimated Casimir energy computed through inverse-free Krylov subspace method with subspace recycled (solid blue triangles), standard Arnoldi method with subspace recycled (solid red circles), asymptotic series (solid black squares) and the extrapolation values. For both efficient methods introduced in Section 4, the dimension of the Krylov subspace is set as $m = 100$. In addition, in the recycling process, only the eigenvectors associated with the extreme eigenvalues whose logarithm is larger than 10^{-5} would be extracted and recycled. With these settings, these two methods with subspace recycled can achieve at least three significant digits accuracy on approximating the Casimir energy.

³The normalized Casimir energy is $\mathcal{E}/\hbar c$, for \mathcal{E} defined in (8).

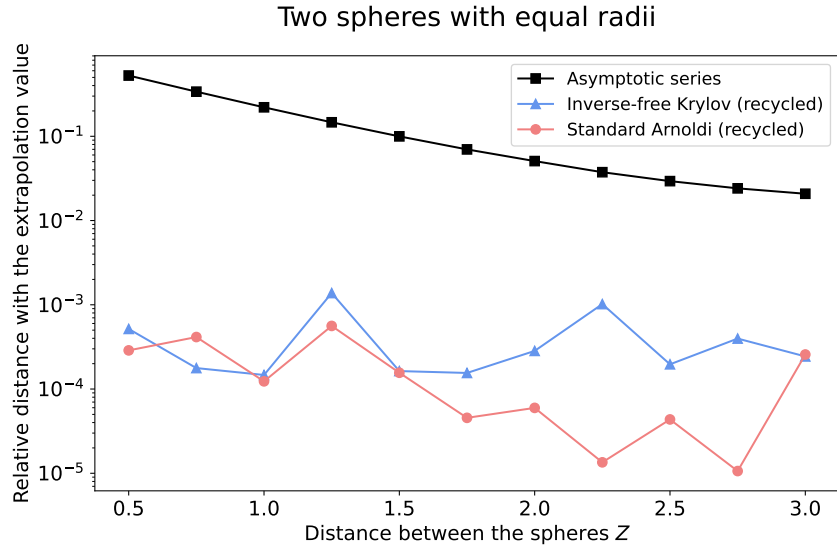


Figure 7: Relative distance between the reference value (computed by Richardson extrapolation) with the asymptotic series (solid black square) and the estimates evaluated from the standard Arnoldi method with subspace recycled (solid red circles) and inverse-free Krylov subspace method with subspace recycled (solid blue triangles). The dimension of the Krylov subspace as $m = 100$.

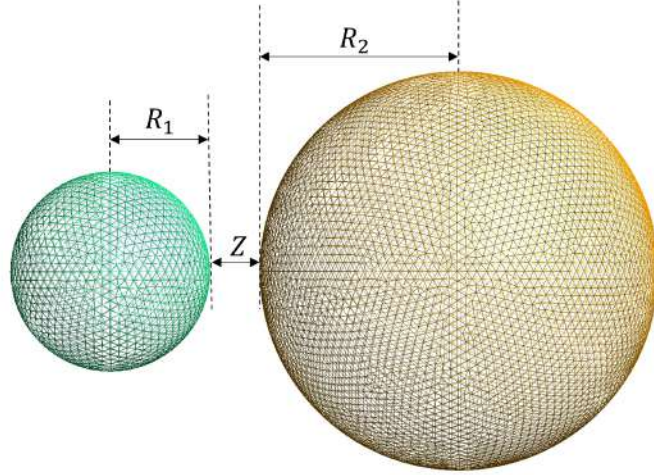


Figure 8: Two spheres with unequal radii: R_1 and R_2 represent the radius of the spheres and Z is the distance between them.

When the perfectly conducting spheres have different radii R_1 , R_2 (see Figure 8), one can still use the asymptotic expansion (19) to determine the upperbound of the integration in the Casimir energy formula.

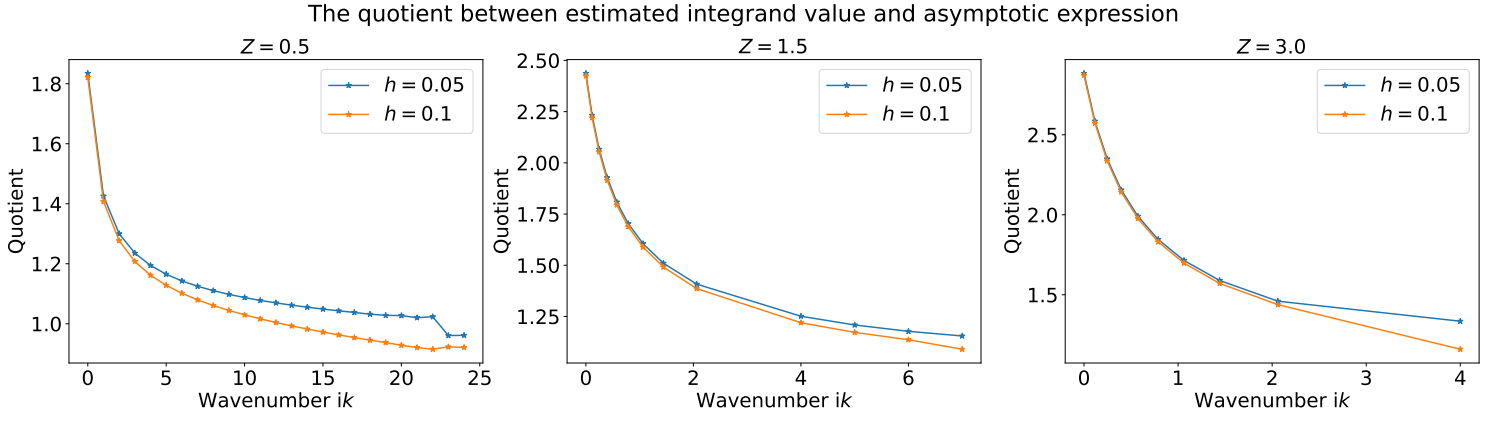


Figure 9: Absolute distance between the approximated integrand value of the Casimir energy formula and the first term in asymptotic expansion (19), and compare this value with the exponential $e^{-2Z\text{Im}k}$. The radii of the spheres are equal to $R_1 = 1$ and $R_2 = 0.5$, and the minimal distance Z between them is 0.5, 1.5 and 3.0. The absolute distance is in solid blue triangles when grid size $h = 0.1$ and in solid orange circles when $h = 0.05$.

Again, with Figure 9, one can easily estimate the upperbound and the results are listed in Table 4.

Distance Z	0.5	0.75	1.0	1.25	1.5	1.75	2.0	2.25	2.5	2.75	3.0
Upperbound	24i	17i	13i	9i	7i	6i	6i	5i	5i	4i	4i

Table 4: The estimated upperbound for the Casimir energy formula for different minimal distance Z varying from 0.5 to 3.0.

By recalling the Remark 2, in order to have at least three significant digits matching with the exact value of the Casimir energy, the upperbound can be set as:

Distance Z	0.5	0.75	1.0	1.25	1.5	1.75	2.0	2.25	2.5	2.75	3.0
Upperbound	10i	6i	6i	4i	4i	3i	3i	3i	3i	3i	3i

Table 5: The estimated upperbound for the Casimir energy formula for different minimal distance Z varying from 0.5 to 3.0.

Afterwards, by denoting the centre distance as $L = R_1 + R_2 + Z$, the asymptotic expansion of the Casimir energy at asymptotically large distance can be written as:

$$\mathcal{E} = -\frac{\hbar c}{\pi} \frac{1}{L} \sum_{n=0}^{\infty} \tilde{b}_n(\eta) \left(\frac{R_1}{L} \right)^{n+2}, \quad (21)$$

where the coefficients $\{\tilde{b}_n\}$ depend on the parameter $\eta = R_2/R_1$ and the first six coefficients are

$$\begin{aligned} \tilde{b}_0 &= -\frac{\eta}{4}, & \tilde{b}_1 &= -\frac{\eta + \eta^2}{8}, & \tilde{b}_2 &= -\frac{34(\eta + \eta^3) + 9\eta^2}{48}, & \tilde{b}_3 &= -\frac{2(\eta + \eta^4) + 23(\eta^2 + \eta^3)}{32}, \\ \tilde{b}_4 &= -\frac{8352(\eta + \eta^5) + 1995(\eta^2 + \eta^4) + 38980\eta^3}{5760}, & \tilde{b}_5 &= -\frac{-1344(\eta + \eta^6) + 5478(\eta^2 + \eta^5) + 2357(\eta^3 + \eta^4)}{2304}. \end{aligned}$$

In the following experiment, the radii of the spheres shown in Figure 8 are set as $R_1 = 0.5$ and $R_2 = 1$. As in the previous example, the exact value of the Casimir energy is computed through the Richardson extrapolation formula (18), where the coarse and fine grid size are $h_{\text{fine}} = 0.05$ ($\dim(\mathbf{V}_{ik}) = 7893$) and $h_{\text{coarse}} = 0.1$ ($\dim(\mathbf{V}_{ik}) = 2023$), separately.

In this case, the asymptotic value of the Casimir energy was estimated by the series (21) and the comparison between the exact value and asymptotic one is shown in Figure 10. Again, one can notice that when the distance between two spheres decreases, the asymptotic value gets close to the exact one and the reason for this is clearly stated in the above equal radii's case.

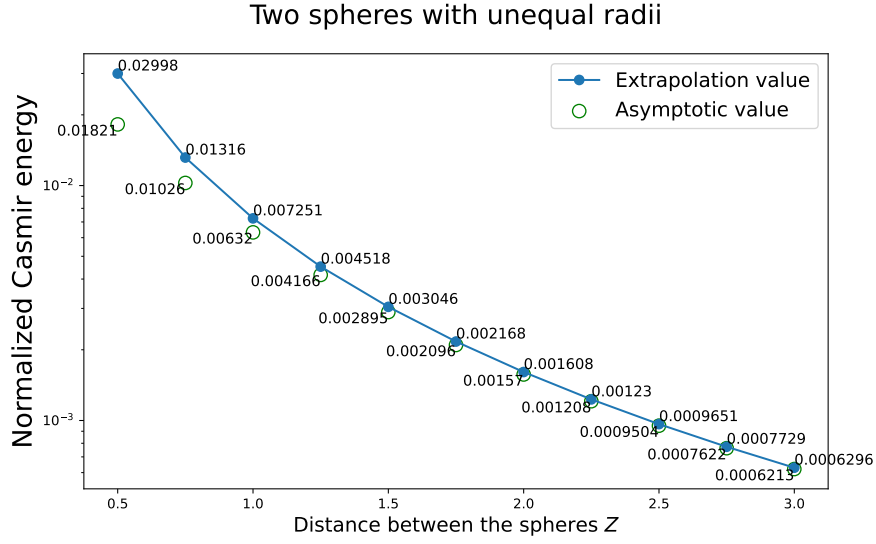


Figure 10: Normalized Casimir energy in two spheres with unequal radii's case. The radius is $R = 1$ and the distance Z ranges from 0.5 to 3.0. The exact value of the (normalized) Casimir energy has been written beside the data point, which is round up to 4 significant digits.

By keeping all the experimental settings being the same with the equal radii's case, the numerical experiments on testing the performance of the inverse-free and standard Arnoldi methods with subspace recycled have been done in the unequal radii's case and the results are shown in Figure 11.

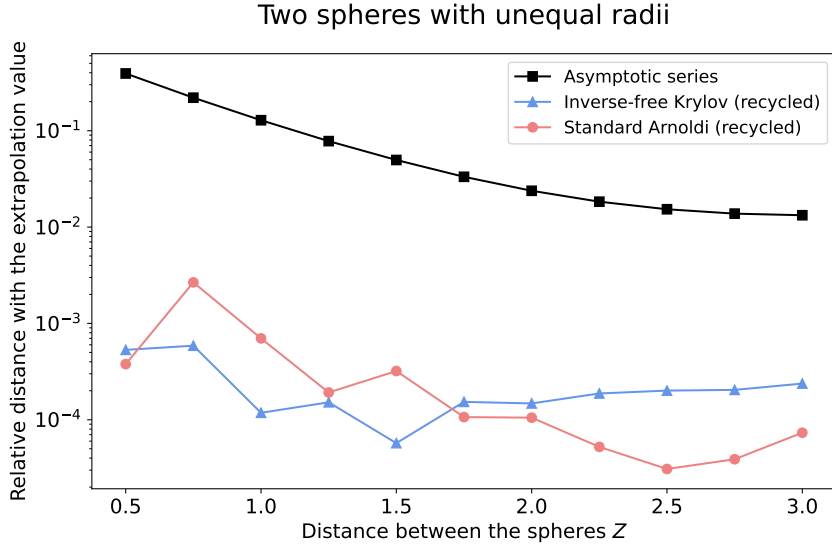


Figure 11: Relative distance between the reference value (computed by Richardson extrapolation) with the asymptotic series (solid black square) and the estimates evaluated from the standard Arnoldi method with subspace recycled (solid red circles) and inverse-free Krylov subspace method with subspace recycled (solid blue triangles). The dimension of the Krylov subspace as $m = 100$.

5.2. Realistic objects case

In this part, the Casimir energy between the objects with special shapes such as the menger sponges, ice crystals and ellipsoids will be computed through the Richardson extrapolation mentioned in the beginning of this section and the values labelled in the following figures are always round up to 4 significant digits.

Figure 12 plots the menger sponges in different levels (0, 1 and 2) and the length of these sponges is always 1. Afterwards, the Casimir energy between two menger sponges in the same level are listed in Table 6. In addition, inside the extrapolation process, when $h_{\text{coarse}} = 0.05$, the $\dim(V_{ik}) = 5672, 8510$ and 27136 and when

$h_{\text{fine}} = 0.1$, the $\dim(V_{ik}) = 1482, 3092$ and 14464 in different level (0, 1 and 2) cases, separately. By comparing the data point in this table, it is easy to find that the Casimir energy decreases as the number of the iteration increases since the cross-sectional area gets smaller.

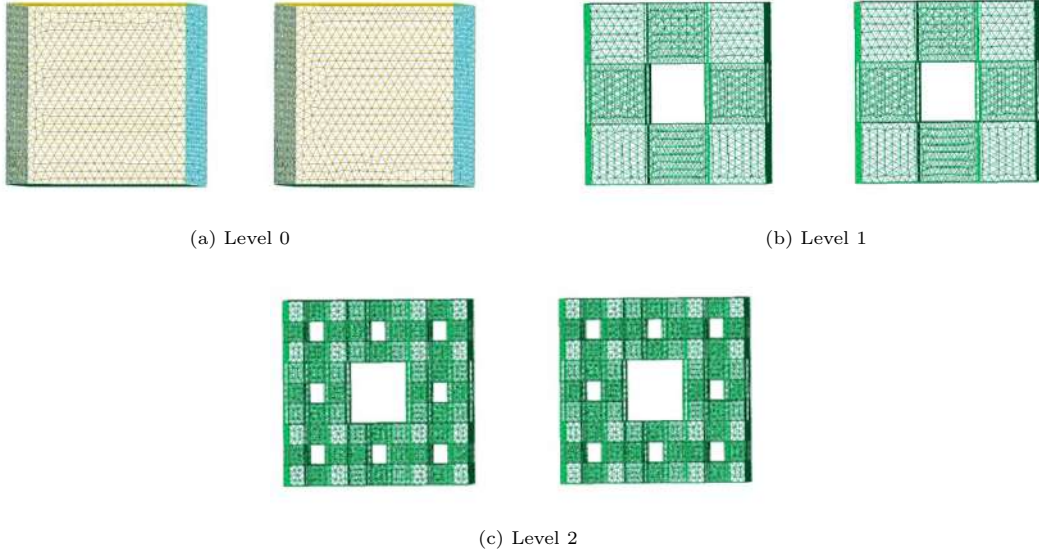


Figure 12: Menger sponges in different levels. The length of each sponge is 1.

Normalized Casimir energy in two menger sponges' case			
Distance	Level 0	Level 1	Level 2
0.5	0.08352	0.080737	0.07979
0.75	0.02735	0.02686	0.02669
1.0	0.01305	0.1288	0.01282
1.25	0.007358	0.007281	0.007253
1.5	0.004607	0.004568	0.004551
1.75	0.003099	0.003076	0.0030658
2.0	0.002196	0.002181	0.002174
2.25	0.001619	0.001609	0.001604
2.5	0.001231	0.001224	0.00122
2.75	0.0009599	0.0009546	0.000952
3.0	0.0007644	0.0007603	0.0007583

Table 6: Normalized Casimir energy in two menger sponges' case

In the next example, the scatterers are ice crystals with different number of branches ranging from 2 to 6 (see Figure 13). By Figure 14, when the number of branches increases from 2 to 4, the Casimir energy increases as expected. But when the branches number added up to 5 and 6, the Casimir energy is much smaller since the main cross-sectional part cannot be as close as the 2, 3, 4-branches cases.

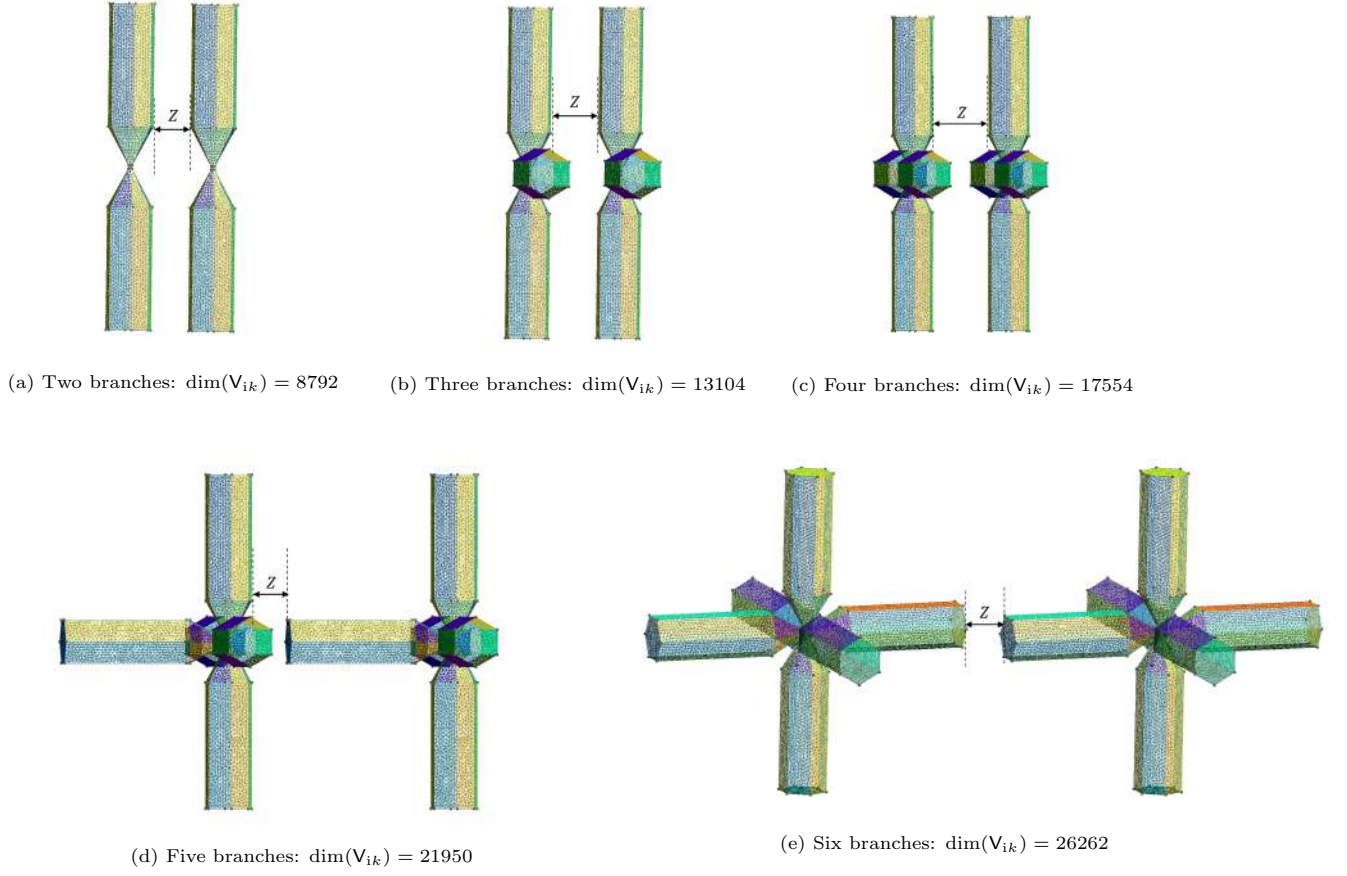


Figure 13: Ice crystals with different number of branches

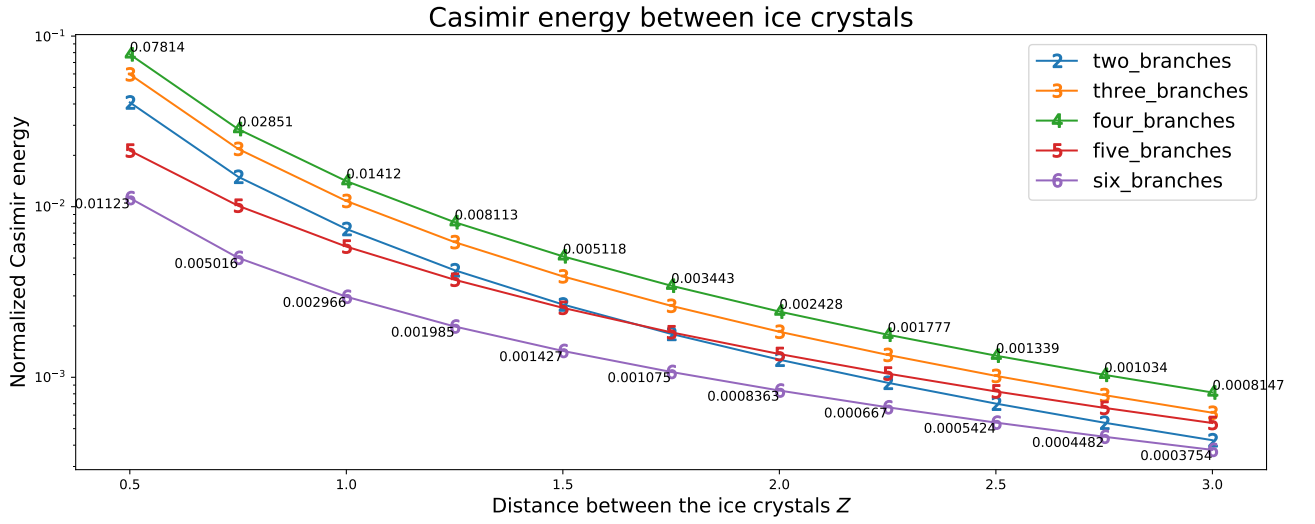


Figure 14: Normalized Casimir energy in ice crystals' case. To make the figure keep clear, only the 4-branches and 6-branches's case data points are labelled in the figure. Other cases' information are listed in Table 7.

Normalized Casimir energy in ice crystals' case					
Distance	2-branches	3-branches	4-branches	5-branches	6-branches
0.5	0.04085	0.05963	0.07814	0.02131	0.01123
0.75	0.01498	0.02182	0.02851	0.01013	0.005016
1.0	0.007403	0.010803	0.01412	0.005834	0.002966
1.25	0.004242	0.006199	0.008113	0.003730	0.001985
1.5	0.002672	0.003905	0.005118	0.002553	0.001427
1.75	0.001268	0.002624	0.003443	0.001835	0.001075
2.0	0.002196	0.001850	0.002428	0.001369	0.0008363
2.25	0.0009290	0.001353	0.001777	0.001051	0.0006670
2.5	0.0007010	0.001019	0.001339	0.0008261	0.0005424
2.75	0.0005420	0.0007867	0.001034	0.0006621	0.0004482
3.0	0.0004277	0.0006198	0.0008147	0.0005394	0.0003754

Table 7: Normalized Casimir energy in two ice crystals' case

It is not hard to imagine that the Casimir energy would be different after the scatterers rotate while keeping the distance between them unchanged. Therefore, in the last example, we would see how the Casimir energy between two identical ellipsoids changes as one of the ellipsoids rotates.

In Figure 15a, the above ellipsoid is centering at $(0, 0, 0)$ and the points $(0.5, 0, 0)$, $(0, 1, 0)$ and $(0, 0, 0.5)$ are located on this surface and if the distance between these two ellipsoids is denoted as Z , then the below one is centering at $(0, 0, -(0.5 + 0.5 + Z))$ and the points $(0.5, 0, -(0.5 + 0.5 + Z))$, $(0, 1, -(0.5 + 0.5 + Z))$ and $(0, 0, 0.5 - (0.5 + 0.5 + Z))$ are on it. Without rotation, the Casimir energy between them with different distance Z is plotted in Figure 16a.

To explore how the rotation affects the change of the Casimir energy, one can always keep one ellipsoid fixed and rotate the other one. The Figure 15b and 15c describe the case when one of the ellipsoids rotates around z - and x -axis, respectively. From the Figure 16b, the Casimir energy changes periodically since we rotate one ellipsoid around z - or x -axis by 360 degrees.

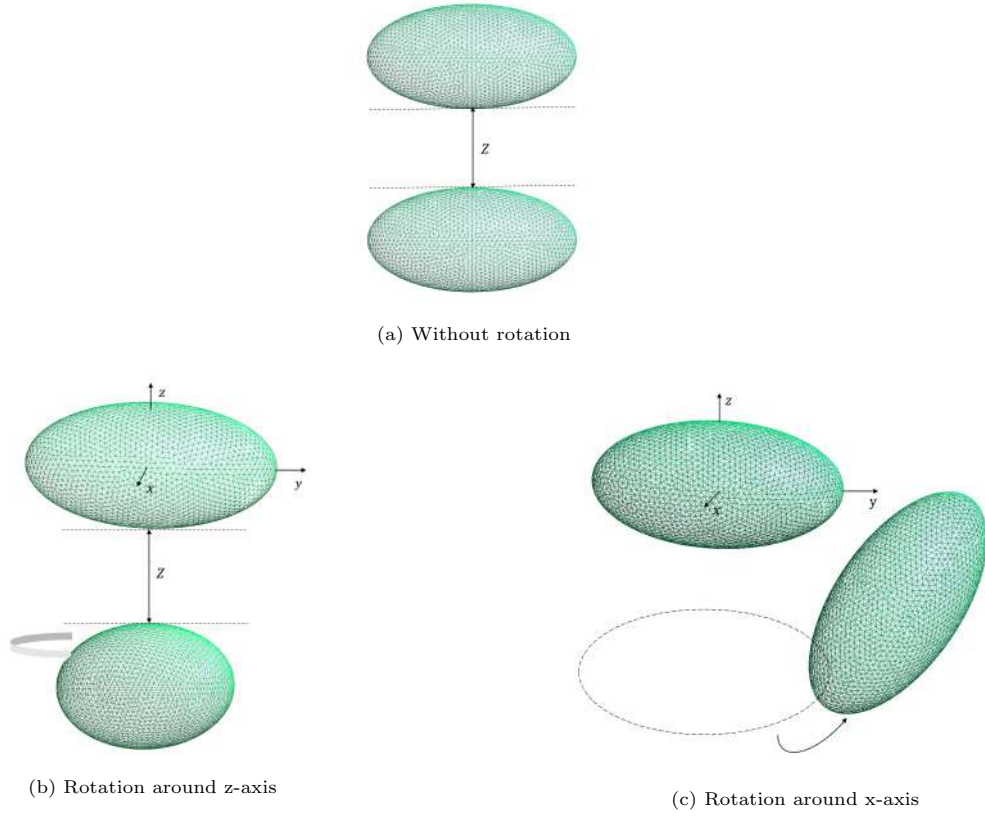
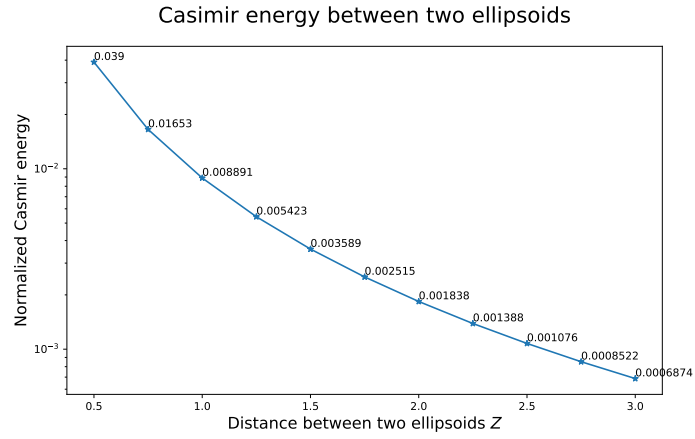
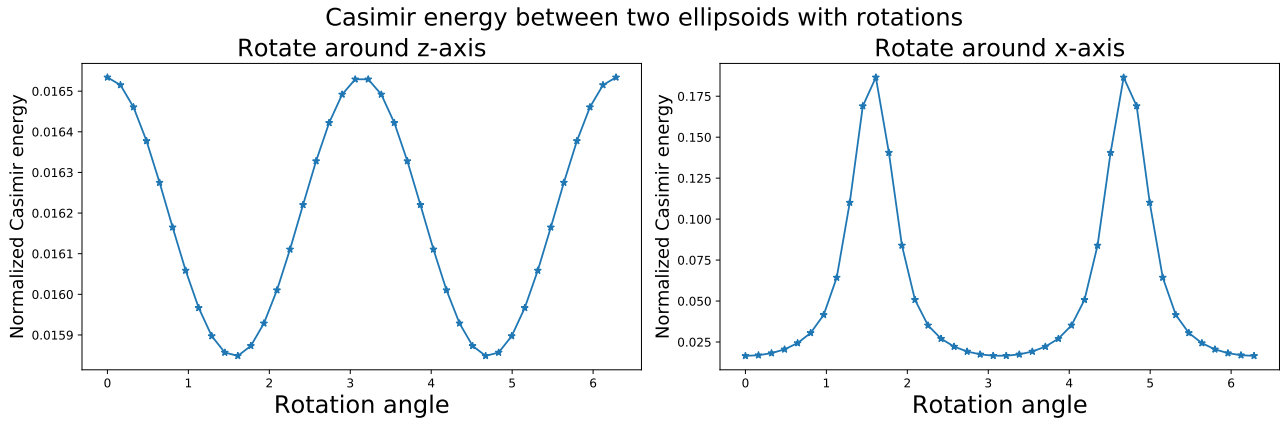


Figure 15: Two ellipsoids with or without rotation: when $h_{\text{fine}} = 0.05$, $\dim(V_{ik}) = 5517$; $h_{\text{coarse}} = 0.1$, $\dim(V_{ik}) = 3509$.



(a) Casimir energy between two ellipsoids with different distances



(b) Casimir energy when one of the ellipsoids rotates

Figure 16: The dependence of the Casimir energy and rotation angle of one of the ellipsoids.

Now, consider 4 ellipsoids located on the vertices of a regular tetrahedron with edge length 2 (Figure 17) and the principal semi-axes of all these ellipsoids are $r_1 = 0.6$ and $r_2 = 0.3$. Figure 17b and Figure 17c show the rotation of the ellipsoids inwards and outwards 360 degrees towards the centroid of this tetrahedron, separately. Afterwards, in order to use the Richardson extrapolation method to estimate the Casimir energy, we evaluate the integral (8) with the grid size set as $h_{\text{fine}} = 0.05$ and $h_{\text{coarse}} = 0.03$. Note that the number of the scatterers has increased to four, the matrices V_{ik} and \tilde{V}_{ik} have become to 4 by 4 block and diagonal block matrix, respectively. From the Figure 18, it shows that the Casimir energy between these four ellipsoids changes periodically with the rotation.

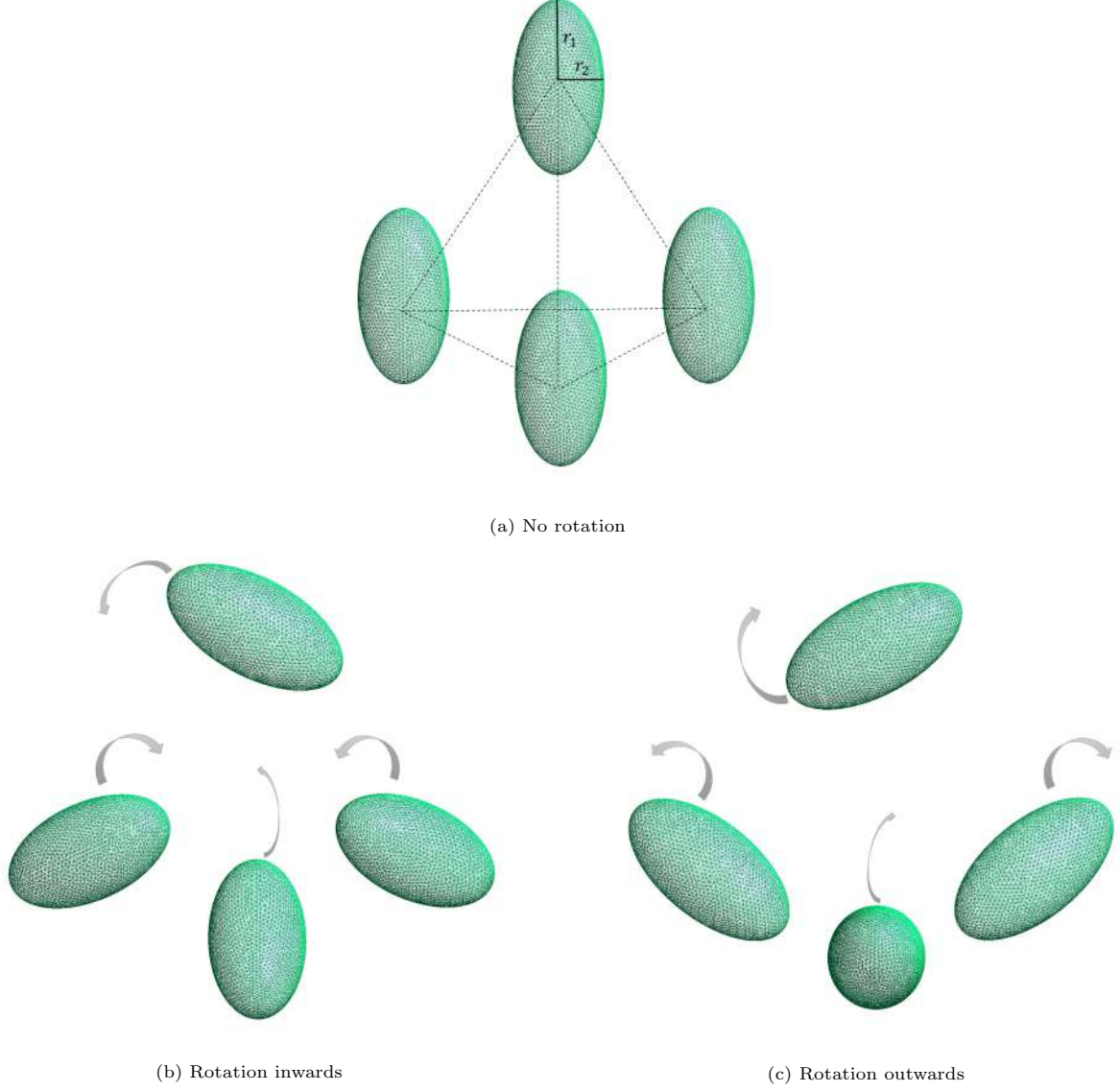


Figure 17: Four ellipsoids with or without rotations: when $h_{\text{fine}} = 0.03$, $\dim(V_{ik}) = 11024$; $h_{\text{coarse}} = 0.05$, $\dim(V_{ik}) = 4160$.

Casimir energy between four ellipsoids with rotation

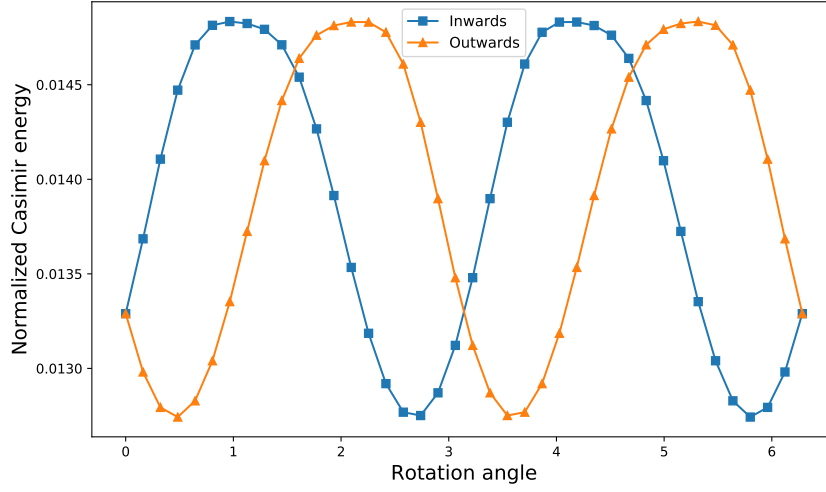


Figure 18: The dependence of the Casimir energy and rotation angle of one of the ellipsoids. Inwards towards the centroid case (solid blue square). Outwards towards the centroid case (solid orange triangle).

The scatterers of the last example are described inside the Figure 19. These six ellipsoids located on the vertices of a regular octahedron with edge length 2 and again the principal semi-axes of all these ellipsoids are $r_1 = 0.6$ and $r_2 = 0.3$ (shown in the Figure 19). This time, the ellipsoids rotate inwards and outwards 360 degrees towards the centroid of this octahedron (Figure 19b and Figure 19c). By closely looking at these two rotation figures, we can notice that Figure 19b can be obtained by rotating Figure 19c 180 degrees. Therefore, the Casimir energies for the inwards and outwards cases are the same. Figure (20) shows how the Casimir energy changes among these six ellipsoids as they rotate.

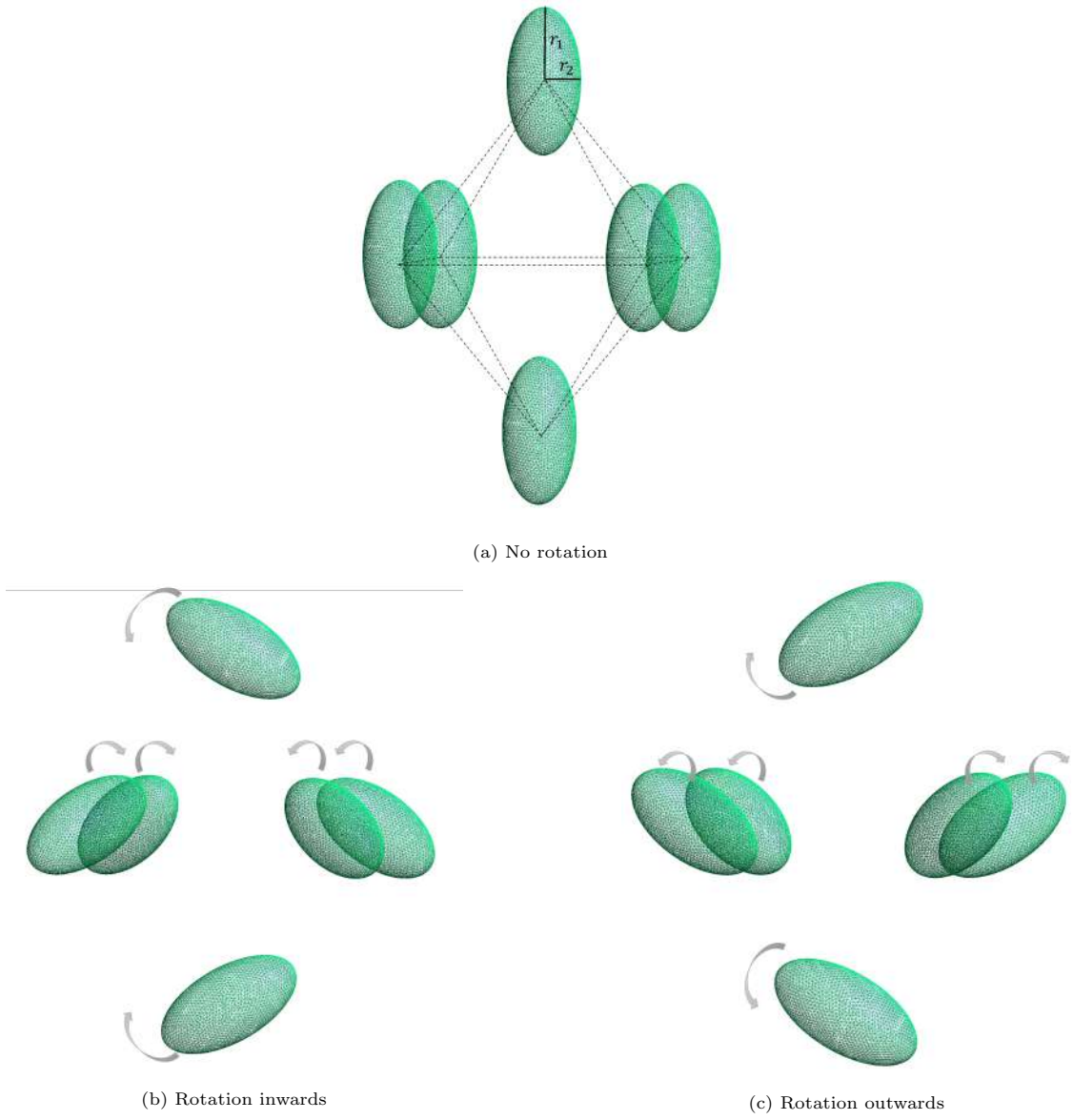


Figure 19: Six ellipsoids with or without rotations: when $h_{\text{fine}} = 0.03$, $\dim(V_{ik}) = 16536$; $h_{\text{coarse}} = 0.05$, $\dim(V_{ik}) = 6240$.

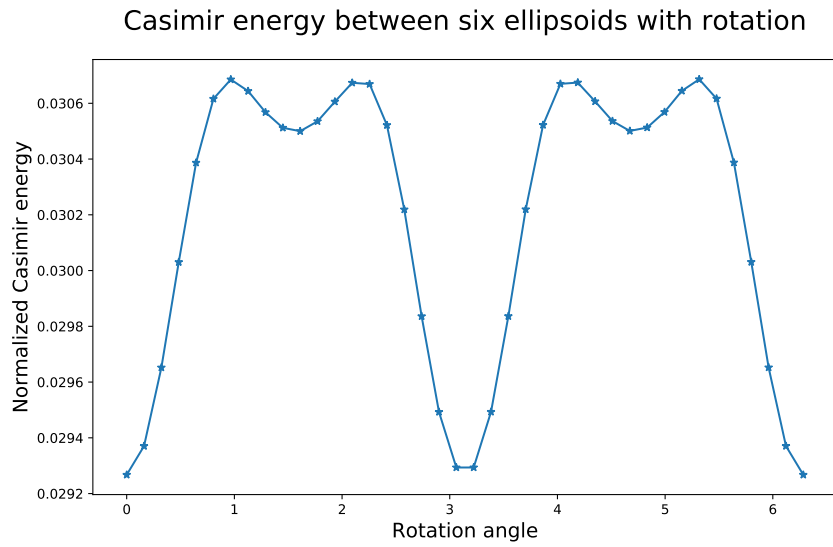


Figure 20: The dependence of the Casimir energy and rotation angle of one of the ellipsoids.

6. Conclusion

References

References

- [1] H. B. Casimir, On the attraction between two perfectly conducting plates, in: Proc. Kon. Ned. Akad. Wet., Vol. 51, 1948, p. 793.
- [2] I. E. Dzyaloshinskii, E. M. Lifshitz, L. P. Pitaevskii, The general theory of van der waals forces, *Advances in Physics* 10 (38) (1961) 165–209.
- [3] S. K. Lamoreaux, Demonstration of the casimir force in the 0.6 to 6 μ m range, *Physical Review Letters* 78 (1) (1997) 5.
- [4] T. Ederth, Template-stripped gold surfaces with 0.4-nm rms roughness suitable for force measurements: Application to the casimir force in the 20–100-nm range, *Physical Review A* 62 (6) (2000) 062104.
- [5] G. Bressi, G. Carugno, R. Onofrio, G. Ruoso, Measurement of the casimir force between parallel metallic surfaces, *Physical review letters* 88 (4) (2002) 041804.
- [6] D. Krause, R. Decca, D. López, E. Fischbach, Experimental investigation of the casimir force beyond the proximity-force approximation, *Physical review letters* 98 (5) (2007) 050403.
- [7] H. B. Chan, Y. Bao, J. Zou, R. Cirelli, F. Klemens, W. Mansfield, C. Pai, Measurement of the casimir force between a gold sphere and a silicon surface with nanoscale trench arrays, *Physical review letters* 101 (3) (2008) 030401.
- [8] T. Emig, N. Graham, R. Jaffe, M. Kardar, Casimir forces between compact objects: The scalar case, *Physical Review D* 77 (2) (2008) 025005.
- [9] T. Emig, N. Graham, R. Jaffe, M. Kardar, Casimir forces between arbitrary compact objects, *Physical review letters* 99 (17) (2007) 170403.
- [10] M. H. Reid, A. W. Rodriguez, J. White, S. G. Johnson, Efficient computation of casimir interactions between arbitrary 3d objects, *Physical review letters* 103 (4) (2009) 040401.
- [11] F. Hanisch, A. Strohmaier, A. Waters, A relative trace formula for obstacle scattering, *arXiv preprint arXiv:2002.07291* (2020).
- [12] M. W. Scroggs, T. Betcke, E. Burman, W. Śmigaj, E. van’t Wout, Software frameworks for integral equations in electromagnetic scattering based on calderón identities, *Computers & Mathematics with Applications* 74 (11) (2017) 2897–2914.
- [13] P. Waterman, New formulation of acoustic scattering, *The journal of the acoustical society of America* 45 (6) (1969) 1417–1429.
- [14] M. Ganesh, S. C. Hawkins, A far field based t-matrix method for three dimensional acoustic scattering, *ANZIAM Journal* 50 (2008) 121–136.

- [15] Y. Nakatsukasa, Off-diagonal perturbation, first-order approximation and quadratic residual bounds for matrix eigenvalue problems, in: International Workshop on Eigenvalue Problems: Algorithms, Software and Applications in Petascale Computing, Springer, 2015, pp. 233–249.
- [16] G. H. Golub, Q. Ye, An inverse free preconditioned krylov subspace method for symmetric generalized eigenvalue problems, SIAM Journal on Scientific Computing 24 (1) (2002) 312–334.
- [17] J. H. Money, Q. Ye, Algorithm 845: Eigfp: A matlab program for solving large symmetric generalized eigenvalue problems, ACM Transactions on Mathematical Software (TOMS) 31 (2) (2005) 270–279.
- [18] Y. Saad, Numerical methods for large eigenvalue problems: revised edition, SIAM, 2011.
- [19] Y.-L. Fang, A. Strohmaier, Singularity traces in obstacle scattering and the poisson relation for the relative trace, arXiv preprint arXiv:2104.01017 (2021).